FACULTY
OF MATHEMATICS
AND PHYSICS
Charles University

MASTER THESIS

Kamila Moriová

Investigation of photodissociation dynamics implementing the velocity map imaging technique

Department of Chemical Physics and Optics

Supervisor of the master thesis:	doc. Mgr. Michal Fárník, Ph.D., DSc.
Consultant of the master thesis:	Mgr. Ivo Vinklárek
Study programme:	Physics
Study branch:	Optics and Optoelectronics

Prague 2021

I declare that I carried out this master thesis independently, and only with the cited sources, literature and other professional sources. It has not been used to obtain another or the same degree.

I understand that my work relates to the rights and obligations under the Act No. 121/2000 Sb., the Copyright Act, as amended, in particular the fact that the Charles University has the right to conclude a license agreement on the use of this work as a school work pursuant to Section 60 subsection 1 of the Copyright Act.

In .... date ....

Author's signature

I would like to thank Michal Fárník for his advices and guidance through the thesis process, and for showing me the beauty of science since 2013, for which I am extremely grateful. Next I would also like to thank Ivo Vinkárek and Jozef Rakovský for their time and patience in answering all my questions. The other members of the Department of Dynamics of Molecules and Clusters also deserve my thanks for creating inspiring and friendly atmosphere. In the end I would like to thank my family and friends for their endless love and support.

Title: Investigation of photodissociation dynamics implementing the velocity map imaging technique

Author: Kamila Moriová

Department: Department of Chemical Physics and Optics

Supervisor: doc. Mgr. Michal Fárník, Ph.D., DSc., Department of Dynamics of Molecules and Clusters, J. Heyrovský Institute of Physical Chemistry of the CAS

Abstract: The aim of this thesis is to investigate the effects of change in the chain length and chlorine group position on C–Cl bond photodissociation dynamics of chloroalkanes using the velocity map imaging (VMI) method. Three different chloroalkanes are studied (1-chloropropane, 2-chloropropane, 1-chloropentane) and compared with previously investigated chloromethane. Regardless of the parent chloroalkane, measured kinetic energy distributions (KEDs) of chlorine photofragments exhibit a single peak at energy around 0.8 eV. Photodissociation of higher chloroalkanes involves a recoil of a semi-rigid alkyl fragment, whose internal energy absorbs 40-60% of the total available energy. For chloromethane, however, only less than 10% of the available energy goes into the alkyl fragment excitation. Measured results of the energy partitioning are compared with calculations based on classical impulsive models. VMI experiment in combination with theory also yields information about the nature of electronic transition and probability of the intersystem crossing. Analysis indicates that the direct absorption into the triplet state is more probable for the chloroalkanes with longer chain length, especially for the branched one.

Keywords: molecular beams, photodissociation, velocity map imaging, dynamics of elementary molecular processes, atmospheric chemistry

Contents

Introduction

Behind every chemical reaction there are dozens of elementary processes. Even though the chemistry of practical interest usually takes place in the bulk material, in order to understand the mechanism and dynamics of reaction in detail, we need to look at the molecular level. A huge progress in this direction came with the development of atomic and molecular beams. The possibility of the investigation of reactions between isolated molecules provides insight into the mechanism of elementary processes. However, such elementary reactions are devoid of secondary processes, and thus do not tell us much about the chemistry in the condensed matter, where all the processes are strongly influenced by the solvent molecules. Fortunately, there is a bridge between the chemistry of the isolated molecules and the chemistry of the bulk so that we can study the reactions of molecules in their solvation environment while still remaining at the molecular level. This bridge is called cluster. Clusters are weakly bound assembly of molecules, atoms, and in some cases ions. Definition includes all the aggregates from dimers to conglomerates of thousands of constituents, which are often called nanoparticles [Castleman, 1990, Fárník, 2011, Fárník et al., 2021, Jena and Castleman, 2006].

In this thesis, we are primarily interested in the particles and processes relevant to atmospheric chemistry and physics. Until recently, scientists were mainly concerned with atmospheric processes taking place in the gas phase. However, the surprising discovery of the Antarctic ozone hole in the mid-1980s and subsequent intensive research has revealed the importance of heterogeneous chemistry (in which reactants consists of different phases) of atmospheric aerosols [Douglass et al., 2014]. Therefore, to reach a detail understanding of atmospheric processes, we need to consider both gas phase reactions and heterogeneous reactions inside or on the surface of aerosol particles. In the laboratory, we can use the molecular beam technique to create single molecules (in seeded expansions) or clusters similar to aerosols, and mimic the processes that take place in the atmosphere.

This work focuses on the photodissociation dynamics of three higher chloroalkanes of different chain length and geometry (1-chloropropane, 2-chloropropane and 1-chloropentane), and its comparison with previously measured photodissociation dynamics of chloromethane (molecule, which was responsible for nearly 17% of the ozone-destroying chlorine in the atmosphere in 2008 [Fahey and Hegglin, 2011], and is expected to control the future abundances of stratospheric ozone [Bahlmann et al., 2019, Cristofanelli et al., 2020]). Some recent studies pointed out that the increasing structural complexity of the molecules influences the photodissociation dynamics [Corrales et al., 2014] and alignment when adsorbed on water droplets [Pasalic et al., 2011]. Therefore, it is of high interest to study the effects of the chain prolongation and the change in chlorine group position on the photodynamics of chloroalkanes.

Molecular beam experiments allow us to study the dynamics of elementary processes in molecules upon photodissocition, which is the motor for any chain reaction is the atmosphere, creating radical fragments. In its very nature, photodissociation is a anisotropic vector process, and information about the dynamics can be accessed using the velocity map imaging (VMI) technique.

The goals of this work are: first, measure the test system (HBr) and calibrate the VMI implemented on the Apparatus for IMaging (AIM) built at J. Heyrovský Institute, second, measure and analyse the photodissociation dynamics of Cl-containing molecules exploiting the Cl fragment detection, and third, compare the measured results with classical mechanics models.

Obtained results will be the basis for further measurements of the chloroalkanes picked-up on ice nanoparticles, simulating the atmospheric aerosols.

1. Photochemistry of molecules and clusters

1.1 Atmospheric chemistry and ozone depletion

1.1.1 Aerosols

The chemistry of Earth's atmosphere is, of course, influenced by its composition, which changes as result of natural processes and human activity. One of the significant influences are aerosols, which could be described as suspensions of solid or liquid (or a mixture of both condensed phases) droplets in a gas. In the atmosphere, aerosols are scattering and absorbing solar radiation, serving as a condensation nuclei for cloud droplet formation and also influencing the chemistry through heterogeneous interactions. They are in the interest of research as they are involved in various environmental issues, for example climate change, acid rain, air pollution (smog) or ozone depletion. Diameters of aerosols range from just a few nanometres up to $20\,\mu$m for cloud particles or ice crystals. Primary aerosols, which are emitted into the atmosphere directly from the Earth's surface, come from both natural and human sources. Dust and sea salts can be an example of the former source, particles from industrial and vehicle pollution are an example of the latter. Another type of aerosols are secondary aerosols, which are formed in the atmosphere. [Kolb and Worsnop, 2012]

Aerosol particles play a crucial role in stratospheric ozone depletion as they form polar stratospheric clouds (PSCs) involved in heterogeneous chemistry leading to fast ozone destruction, as will be discussed further. In the simplest case, PCS can be divided into two types: the common type contains nitric acid (HNO_3), sulfuric acid (H_2SO_4) and water, the rare type consists of water ice only [Peter, 1997, Fahey and Hegglin, 2011].

1.1.2 Ozone depletion via gas phase chemistry

Ozone (O_3) is a gas that occurs naturally in Earth's atmosphere. It can be found mostly in the stratosphere [Fahey and Hegglin, 2011], which is the layer of the atmosphere between ∼12 and 50 km. The temperature of the stratosphere increases with increasing altitude due to the presence of ozone, which absorbs ultraviolet (UV) radiation. The layer between surface and stratosphere is called troposphere, and in contrast its temperature decreases with increasing altitude. [Solomon, 1999]

The presence of ozone in the Earth's stratosphere is of fundamental importance as it has a unique feature among the other atmospheric gases – it absorbs UV radiation from the Sun at wavelengths that are damaging for biologically active molecules [Douglass et al., 2014]. Thus, ozone depletion results in increased UV radiation levels on the Earth's surface, which has an adverse impact on human health [Slaper et al., 1996]. The systematic measurement of ozone abundances, which began in various regions during the first half of the last century, had been showing a gradual significant decrease since around 1980. This revelation made ozone depletion one of the major environmental issues of the last century [Solomon, 1999].

In the stratosphere, ozone is naturally created and destroyed by UV photodissociation following oxygen-only chemical pathways, known as Chapman cycle. This ozone regeneration cycle was proposed in 1930. Later, it turned out that ozone can be also destroyed by other species in catalytic cycles, in particular by chlorine radical:

$$\mathrm{Cl} + \mathrm{O_3} \longrightarrow \mathrm{ClO} + \mathrm{O_2}$$

$$\mathrm{ClO} + \mathrm{O} \longrightarrow \mathrm{Cl} + \mathrm{O_2}.$$

In this ozone destructing cycle, chlorine has a role of catalyst as Cl and ClO are destroyed and recreated. That means a single chlorine atom can participate in many cycles and destroy hundreds of ozone molecules before reacting with other gas and being locked up in the reservoir. During its lifetime in the stratosphere, it can destroy up to ten thousands of ozone molecules. It ought to be mentioned that chlorine-involving catalytic cycles are only one group of many that participate on ozone destruction. However, their impact is enormous, especially because of human activity. [Solomon, 1999, Fahey and Hegglin, 2011]

Naturally, chlorine is not present in the atmosphere in large quantities. For example, sea salts or volcano emissions of HCl can contribute to chlorine abundances in the atmosphere, however, their removal in precipitation is very efficient. In 1974, Mario Molina and Frank Rowland identified man-made chlorofluorocarbons (CFCs) as dominant and growing source of stratospheric chlorine, for which they both received Nobel prize (together with Paul Crutzen, who later recognized the importance of heterogeneous chemistry on speeding up the process of ozone depletion [Nobel Media AB]). CFCs, which were used in many industrial applications at that time, including refrigerants or aerosol propellants, are chemically inert and almost insoluble in water, and may remain in the atmosphere for up to decades or even hundreds of years. Emissions of CFCs disrupt the natural ozone balance, which leads to ozone depletion. The UV photodissociation of CFCs high in the stratospere leads to generation of a highly reactive chlorine radicals. These radicals can engage in further reactions, destroying ozone in catalytic cycles described above or creating reservoir gases HCl and $\mathrm{ClONO_2}$, which are not harmful to ozone:

$$\mathrm{Cl} + \mathrm{CH_4} \longrightarrow \mathrm{HCl} + \mathrm{CH_3}$$

$$\mathrm{ClO} + \mathrm{NO_2} + \mathrm{M} \longrightarrow \mathrm{ClONO_2} + \mathrm{M}.^1$$

In these reservoirs, chlorine is relatively well locked and deactivated, however, it can be reconverted back into active Cl atom in subsequent gas phase reactions. The distribution rates of chlorine between active species and reservoirs turned out to determine Cl and ClO abundances involved in the gas-phase chemistry behind ozone depletion. All the chemistry described takes place primarily in the higher stratosphere at altitudes around 40 km, where there are enough UV photons to

---

[1] Here, M is an inert third body participating in the reaction.

interact with chlorine precursors CFCs. In 1982, predictions were made based on gas phase chemistry and stratospheric circulation that the global abundance of ozone would decrease by less than 10 % in next 100 years. However, in 1985, an unexpected discovery of the Antarctic ozone hole revealed the importance of heterogeneous chemistry on ozone depletion, pushing gas phase chemistry to the background as a minor cause of ozone loss. [Solomon, 1999, Douglass et al., 2014, Molina and Rowland, 1974]

1.1.3 Ozone depletion via heterogeneous chemistry

In October 1985, dramatic ozone depletion was reported over Antarctica. This phenomenon, which became known as the ozone hole, is restricted to the South pole and occurs seasonally during the polar spring. The Antarctic ozone hole discovery was surprising for primarily three reasons. First, such large and sudden depletion was not anticipated. Second, propositions made based on gas phase chemistry expected the greatest depletion around 40 km, but depletion over Antarctica was measured at much lower altitudes. Third, the region of Antarctica was not suspected to be affected by such a massive ozone loss. It was later shown that we need to consider heterogeneous reactions, not only the gas phase ones, to understand the rapid depletion of ozone in Antarctica. [Solomon, 1999, Douglass et al., 2014]

Today, polar stratospheric clouds (PCSs) are well known to play a key role in the chemistry behind the massive ozone depletion over Antarctica. Due to the high dryness, the stratosphere is not suitable environment for cloud formation. Hence, PCSs occur only in the unique meteorological and physical conditions of polar winter. PCSs generally form between ∼12 and 25 km and have cold temperatures below 200 K. On the surface of aerosols inside the PCSs, HCl and $ClONO_2$ reservoirs may react in following way:

$$\mathrm{HCl} + \mathrm{ClONO_2} \rightarrow \mathrm{HNO_3} + \mathrm{Cl_2}.$$

Such heterogeneous reaction can change gas phase chlorine partitioning rate and enhance ozone depletion. The resulting Cl_2 molecule is weakly bound and can be easily broken apart in sunlit air. This means that in polar spring, when the sunlight return to the Antarctica, Cl_2 dissociates rapidly into Cl radical and ozone-destroying catalytic cycle begins. Due to the lack of atomic oxygen in the specific conditions of stratospheric polar vortex in early spring, the classical Cl–ClO catalytic cycle described in the previous section is no longer dominant. It is replaced by catalytic cycle involving formation of Cl_2O_2 and also Cl–Br catalytic cycle, both of which are controlled by visible light and very efficient. Furthermore, the dramatic ozone depletion in Antarctica is enhanced yet for another reason. The heterogeneous reaction on PCSs creates rather inert HNO_3, which condense onto the aerosols and is eventually permanently removed from the stratosphere. As a result, the resupply of NO_2 is suppressed. This means there is less chance for chlorine to deactivate back into ozone-inert reservoir $ClONO_2$. [Solomon, 1999, Douglass et al., 2014, Peter, 1997]

Many proposals have been put forward to stop atmospheric ozone loss, but most of them have practical limitations. It seems that the only way to recover ozone in the stratosphere is to reduce CFCs emissions. In 1987, the Montreal protocol was signed in response to the ozone hole detection and subsequent investigation, and has been controlling the global production of CFCs ever since. The return to the original concentrations of ozone in the stratosphere is, however, a slow process due to CFCs' longevity. [Solomon, 1999, Douglass et al., 2014]

As discussed in this chapter, heterogeneous reactions fundamentally affect atmospheric processes and must be considered in models and projections. Even though we understand the physics and chemistry of PCSs enough to identify the origin of the Antarctic ozone hole, detailed understanding that could help us to predict precisely the situation over the South pole is missing [Peter, 1997]. How can we study the effect of solvent on atmospheric chemistry in laboratory conditions? Using the molecular beam method, we can create water clusters (ice nanoparticles representing cloud droplets), pick up various atmospherically relevant molecules and activate the reaction, for example, by photodissociation or electron ionization.

1.2 Photodissociation dynamics

Chemical reactions in the atmosphere are affected by the constant collisions of atmospheric particles with photons. If absorption occurs and the absorbed photon energy exceeds the binding energy of the weakest bond in the molecule, it can break apart. This process is known as photodissociation.

The resulting photofragments are often radicals which rapidly participate in further reactions. That makes photodissociation the motor for many chain reactions in our atmosphere, including the vital ozone regeneration via Chapman cycle [Schinke, 1993, Solomon, 1999]. On the other hand, free halogen radicals Cl, which destroy the ozone layer in the catalytic cycles, are also products of photodissociation [Solomon, 1999]. Therefore, to comprehend chemistry and physics of the atmosphere, we need to take a closer look at photodissociation in its entirety.

1.2.1 Basic principle

Let us describe the process of photodissociation with an example. Consider AB a parent molecule and A, B its photofragments after dissociation caused by absorption of the photons with energy $\hbar\omega$ and frequency ω. These newborn products can be both atoms or molecules with their own internal degrees of freedom. Then, photodissociation can be described by the equation:

$$\mathrm{AB} + N_{\mathrm{photon}}\hbar\omega \longrightarrow (\mathrm{AB})^* \longrightarrow \mathrm{A}(\alpha) + \mathrm{B}(\beta),$$

where N_{photon} is the number of absorbed photons, $(\mathrm{AB})^*$ denotes the excited complex in the repulsive state before breaking apart and α and β represents the specific internal quantum states of the photodissociation products A and B. Thus, photodissociation can be divided into two steps: absorption and fragmentation. [Schinke, 1993]

The cleavage of a chemical bond in the molecule usually requires a single UV photon or many infrared (IR) photons. In this thesis, we are mainly interested in the former case of UV photodissociation, which is schematically illustrated in Figure 1.1, according to Schinke [1993]. The isolated molecule AB (with zero initial internal energy) is excited by a single UV photon from the ground to a higher electronic state, which is in this case repulsive along the intermolecular coordinate R_{AB}. As a result, the molecule is irreversibly broken apart. Part of the photon energy $\hbar\omega$ is consumed by the A-B bond fission and the rest, the excess energy E_{ex}, is redistributed between the translational energy E_{tr} and internal energy E_{int} of the photofragments (including electronic energy, and for polyatomic fragments also vibrational and rotational energy):

$$E_{\mathrm{ex}} = \hbar\omega - D_0 = E_{\mathrm{tr}} + E_{\mathrm{int}}. \tag{1.1}$$

In the equation, D_0 denotes the dissociation energy required to break the bond. It is measured from the zero-point level of the parent molecule AB to the zero-point level of its photoproducts A and B as shown in Figure 1.1. In order to guarantee the excitation into a single electronic state with energy $E_{\mathrm{f}} = E_{\mathrm{i}} + \hbar\omega$, where E_{i} is the energy of the parent molecule, certain conditions must be fulfilled: UV photodissociation should be realised with long light pulses of low intensity and narrow bandwidth. [Schinke, 1993]

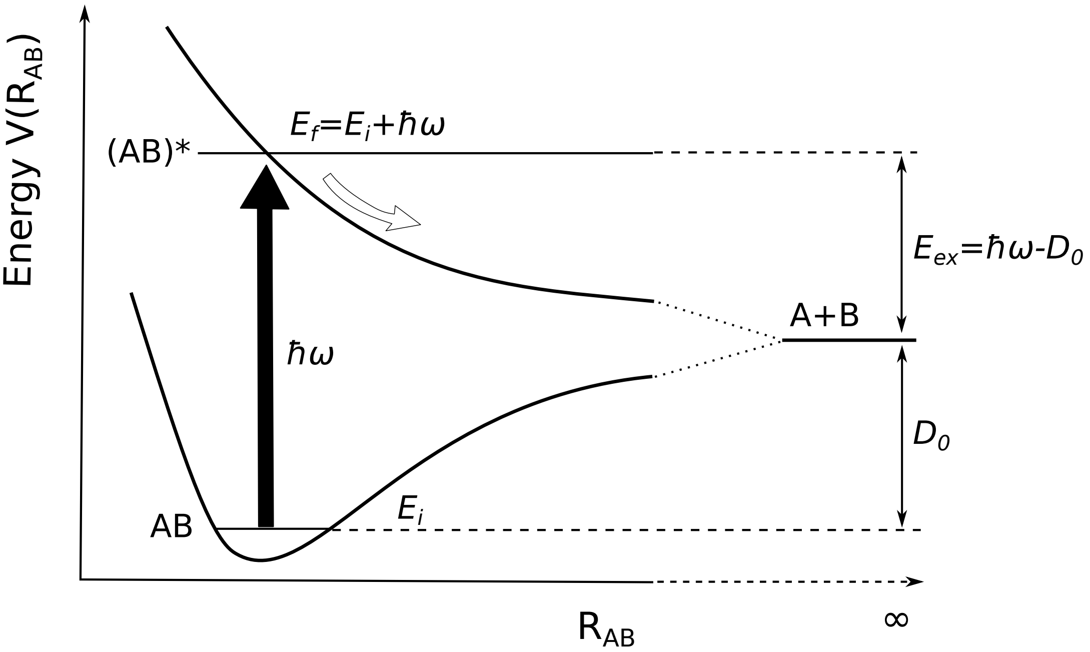

Figure 1.1: Schematic illustration of a single UV photon photodissociation. R_{AB} denotes the intermolecular separation of the two photofragments A and B.

The process shown in Figure 1.1 is the simplest type of direct UV photodissciation. However, photodissociation can be also indirect. The molecule might be excited into a non-repulsive state and then undergo a transition into another one, which is repulsive. Alternatively, the molecule can be excited into a quasi-bound state and prevented from immediate dissociation by the potential barrier. Both of the indirect types of photodissociation are discussed in Schinke [1993]. In practice, we have to deal with the systems with a dense manifold of electronic states and interstate dynamics, which makes it a bit more difficult to understand the result of dissociation.

Let us have a further look on the energy distribution. In the photodissociation process, the excess energy is the total energy available that is redistributed between the translational and internal energy of the photofragments, as already mentioned above. Under our assumption of two body dissociation, which is often the case in the experiment, we can write the total translational energy E_{tr} of the two fragments as

$$E_{\mathrm{tr}} = E_{\mathrm{kin,\,A}} + E_{\mathrm{kin,\,B}} = \frac{p_{\mathrm{A}}^2}{2m_{\mathrm{A}}} + \frac{p_{\mathrm{B}}^2}{2m_{\mathrm{B}}}, \tag{1.2}$$

where $E_{\mathrm{kin,\,A}}$, $E_{\mathrm{kin,\,B}}$ are the kinetic energies, m_{A}, m_{B} are the masses and p_{A}, p_{B} are the momenta of the photofragments A and B.

Within the parent molecule's center-of-momentum frame, we can write the law of conservation of momentum as $0 = \vec{p}_{\mathrm{AB}} = \vec{p}_{\mathrm{A}} + \vec{p}_{\mathrm{B}}$, thus, $\vec{p}_{\mathrm{A}} = -\vec{p}_{\mathrm{B}}$. The momentum conservation together with the equation above yields

$$E_{\mathrm{tr}} = \frac{p_{\mathrm{A}}^2}{2m_{\mathrm{A}}}\left(1 + \frac{m_{\mathrm{A}}}{m_{\mathrm{B}}}\right) = E_{\mathrm{kin,\,A}}\left(1 + \frac{m_{\mathrm{A}}}{m_{\mathrm{B}}}\right). \tag{1.3}$$

After simple modification, we obtain the following formula for the calculation of the total translational energy of the photofragments:

$$E_{\mathrm{tr}} = \frac{m_{\mathrm{AB}}}{m_{\mathrm{B}}} E_{\mathrm{kin,\,A}}, \tag{1.4}$$

where $m_{\mathrm{AB}} = m_{\mathrm{A}} + m_{\mathrm{B}}$ is the mass of the parent molecule.

In our experiment, we measure the velocity of one of the fragments, e.g. fragment A, which means we know its kinetic energy $E_{\mathrm{kin,\,A}}$. As the masses of the constituents of the parent molecule are also known, we can easily calculate the total translational energy E_{tr} and from that also the kinetic energy of the other fragment $E_{\mathrm{kin,\,B}}$. Now let us have a look at the equation 1.1. The energy of the photon $\hbar\omega$ in the experiment is known, as well as the dissociation energy of the bond of the parent molecule D_0. The total translational energy E_{tr} we already calculated, which means we can determine the total internal energy of the fragments E_{int}, the only unknown. Thus, if we know the internal energy of one of the fragments (and that is frequently the case), the internal energy of the other can be counted. In other words, by measuring the velocity of one of the fragments, all the information about the energetics of the photodissociation process can be obtained.

1.2.2 Effect of solvent molecules on photodissociation process

Until now, we have only considered the photodissociation of an isolated molecule. However, understanding the dissociation of a molecule in the environment of another particles is also important. Clusters and nanoparticles of various sizes occur naturally in the atmosphere or in space, where they are fundamentally involved in local chemistry. The question arises: what if the molecule is surrounded by the molecules of solvent? In Figure 1.2, the photodissociation processes of both isolated and solvated molecule AB are schematically illustrated.

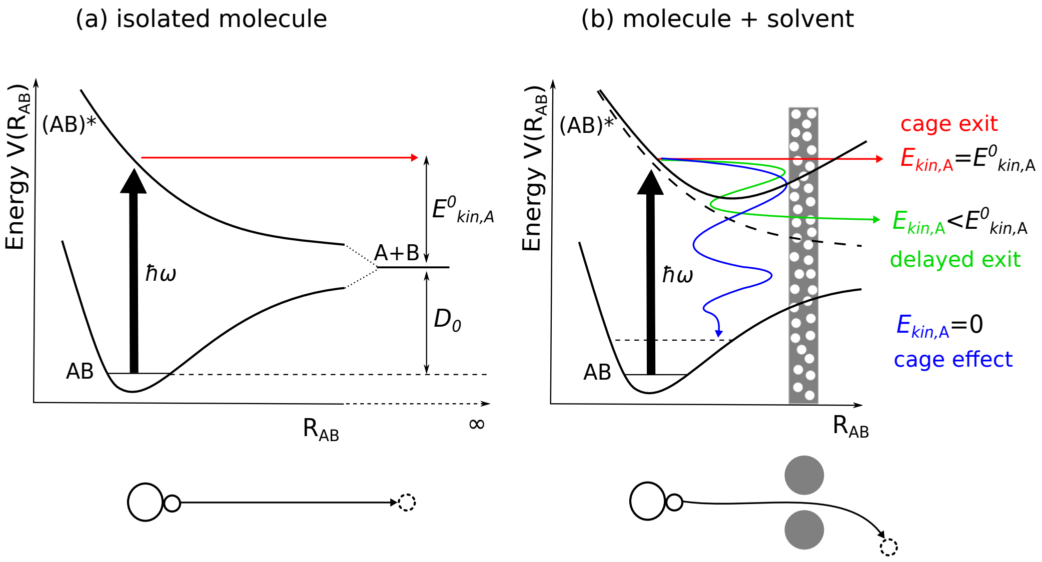
(a) isolated molecule

(b) molecule + solvent

Figure 1.2: Schematic illustration of photodissociation of an isolated molecule AB (a), and a molecule AB surrounded by solvent (b). Image according to Fárník [2011].

In the simple gas phase case, the molecule is excited directly to its higher repulsive potential energy surface (PES) and breaks apart almost immediately. Let us follow the fragment A. After the dissociation, it flies away with the kinetic energy $E^0_{\mathrm{kin,\,A}}$. This process was already described in the previous section. For the molecule in solvated environment, the situation is more complicated because the other molecules prevent its fragments from escaping. In the classical picture, the solvent molecules build a partly transparent wall. Some light and small fragments, for example H from the HBr photodissociation, may tunnel through such wall with its energy unchanged, however, most of the fragments loose at least a part of their energy during the collisions. The influence of solvent molecules can be used, for example, to study the internal excitation of the HBr seeded in He cluster [Fedor et al., 2011]. Within the realistic quantum-mechanical approach, we need to consider the electronic structure of solvent molecules and their interaction with molecule AB. The presence of solvent can close some photodissociation channels and open the new ones. [Fárník, 2011]

1.3 Light-molecule interaction

What influence does a beam of light have on the evolution of a molecular system? In the semiclassical approach, we will treat molecules quantum mechanically and light classically. The time-dependent Schrödinger equation

$$i\hbar \frac{\partial \mathit{\Psi}(\mathbf{Q}, \mathbf{q}; t)}{\partial t} = \hat{H}_0(\mathbf{Q}, \mathbf{q})\, \mathit{\Psi}(\mathbf{Q}, \mathbf{q}; t) \tag{1.5}$$

describes the evolution of the wavefunction $\mathit{\Psi}(\mathbf{Q}, \mathbf{q}; t)$ of some unperturbed molecular system with the time-independent Hamiltonian $\hat{H}_0(\mathbf{Q}, \mathbf{q})$ (taking into account all nuclear and electronic degrees of freedom $\mathbf{Q}$ and $\mathbf{q}$, respectively). The wavefunction can be separated into the stationary wavefunction $\mathit{\Psi}(\mathbf{Q}, \mathbf{q})$, solving the time-independent Schrödinger equation $\hat{H}_0(\mathbf{Q}, \mathbf{q})\mathit{\Psi}(\mathbf{Q}, \mathbf{q}) = E\mathit{\Psi}(\mathbf{Q}, \mathbf{q})$, and a phase factor which depends on time:

$$\mathit{\Psi}_\alpha(\mathbf{Q}, \mathbf{q}; t) = e^{-iE_\alpha t/\hbar}\, \mathit{\Psi}_\alpha(\mathbf{Q}, \mathbf{q}). \tag{1.6}$$

E_α denote eigenenergies. The stationary eigenfunctions $\mathit{\Psi}(\mathbf{Q}, \mathbf{q})$ are orthogonal[1] and satisfy the closure relation[2]. [Schinke, 1993]

For the system under the electromagnetic field, we need to consider the perturbed Hamiltonian $\hat{H}(t) = \hat{H}_0 + \hat{H}_{\text{int}}(t)$, where $\hat{H}_{\text{int}}(t)$ represents the interaction of the light and molecule. In electric dipole approximation, the wavelength of the light is much larger than the molecular dimensions, and thus the whole molecule "feels" the same electric field of light, which can be written as $\mathbf{E}(t) = \mathbf{E}_0 \cos(\omega t)$. The perturbation within the electric dipole approximation is

$$\hat{H}_{\text{int}}(t) = -\hat{\mathbf{d}} \cdot \mathbf{E}_0 \cos(\omega t), \tag{1.7}$$

where $\hat{\mathbf{d}}$ is the electric dipole operator of the molecule. [Schinke, 1993]

The time evolution of the wavefunction of the system with perturbation will now be different. It can be expressed as a linear combination of the stationary eigenfunctions $\mathit{\Psi}_\alpha(\mathbf{Q}, \mathbf{q})$ of the unperturbed system, as they form a basis in the Hilbert space of $\hat{H}_0$. Therefore,

$$\mathit{\Psi}(\mathbf{Q}, \mathbf{q}; t) = \sum_\alpha a_\alpha(t)\, e^{-iE_\alpha t/\hbar}\, \mathit{\Psi}_\alpha(\mathbf{Q}, \mathbf{q}), \tag{1.8}$$

where $a_\alpha(t)$ are the unknown coefficients related to the probability of that the electron occupies given state at given time t, and normalized such that $\sum_\alpha |a_\alpha(t)|^2 = 1$. Substitution of the above wavefunction into the time-dependent Schrödinger equation with perturbed Hamiltonian $\hat{H}(t)$ and some manipulations yield the set of the first-order differential equations describing the evolution of the molecular system interacting with radiation:

$$\frac{\mathrm{d}}{\mathrm{d}t} a_\alpha(t) = \frac{1}{i\hbar} \sum_{\alpha'} h_{\alpha\alpha'} a_{\alpha'}(t) e^{i\omega_{\alpha\alpha'} t}, \tag{1.9}$$

---

[1] $\int \mathrm{d}\mathbf{Q}\, \mathrm{d}\mathbf{q}\, \mathit{\Psi}^*_\alpha(\mathbf{Q}, \mathbf{q})\, \mathit{\Psi}_{\alpha'}(\mathbf{Q}, \mathbf{q}) = \delta_{\alpha\alpha'}$

[2] $\sum_\alpha \mathit{\Psi}_\alpha(\mathbf{Q}, \mathbf{q})\, \mathit{\Psi}^*_\alpha(\mathbf{Q'}, \mathbf{q'}) = \delta(\mathbf{Q} - \mathbf{Q'})\, \delta(\mathbf{q} - \mathbf{q'})$

where $\omega_{\alpha\alpha'} = (E_\alpha - E_{\alpha'})/\hbar$ are transition frequencies and $h_{\alpha\alpha'}$ are the matrix elements of the perturbation operator $\hat{H}_{\text{int}}$,

$$\begin{aligned} h_{\alpha\alpha'} &= \int \mathrm{d}\mathbf{Q}\, \mathrm{d}\mathbf{q}\, \Psi_\alpha^*(\mathbf{Q}, \mathbf{q})\, \hat{H}_{\text{int}}\, \Psi_{\alpha'}(\mathbf{Q}, \mathbf{q}) \\ &= \langle \Psi_\alpha | \hat{H}_{\text{int}} | \Psi_{\alpha'} \rangle \\ &= \langle \Psi_\alpha | -\hat{\mathbf{d}} \cdot \mathbf{E}_0 | \Psi_{\alpha'} \rangle \cos(\omega t) \\ &= d_{\alpha\alpha'} \cos(\omega t), \end{aligned} \tag{1.10}$$

where we defined the time-independent matrix elements as $d_{\alpha\alpha'}$. Combining Equations 1.9 and 1.10 yields

$$\frac{\mathrm{d}}{\mathrm{d}t} a_\alpha(t) = \frac{1}{i\hbar} \sum_{\alpha'} d_{\alpha\alpha'}\, a_{\alpha'}(t)\, \cos(\omega t)\, e^{i\omega_{\alpha\alpha'} t}. \tag{1.11}$$

Assuming electric field to be a weak perturbation to the molecular system, i.e. probabilities $|a_\alpha|^2$ do not change significantly in the presence of light, we can solve this equation by the first-order perturbation theory. For each final state (f), which is now restricted to be coupled to the initial state (i) only, applies:

$$\frac{\mathrm{d}}{\mathrm{d}t} a_{\text{f}}(t) = \frac{1}{i\hbar} d_{\text{fi}}\, \cos(\omega t)\, e^{i\omega_{\text{fi}} t}. \tag{1.12}$$

Substitution $\cos(\omega t) = \frac{1}{2}\left(e^{i\omega t} + e^{-i\omega t}\right)$ and integration gives us

$$a_{\text{f}}(t) = \frac{d_{\text{fi}}}{2\hbar} \left[\frac{1 - e^{i(\omega_{\text{fi}} + \omega)t}}{\omega_{\text{fi}} + \omega} + \frac{1 - e^{i(\omega_{\text{fi}} - \omega)t}}{\omega_{\text{fi}} - \omega} \right]. \tag{1.13}$$

Within the rotating wave approximation we can neglect the term that oscillates rapidly. In the case of absorption ($\omega_{\text{fi}} > 0$), it is the first term which is much smaller:

$$a_{\text{f}}(t) = \frac{d_{\text{fi}}}{2\hbar} \frac{1 - e^{i(\omega_{\text{fi}} - \omega)t}}{\omega_{\text{fi}} - \omega}. \tag{1.14}$$

Now we can determine the probability of transition from the initial to the final state

$$P_{\text{fi}}(t) = |a_{\text{f}}|^2 = \left(\frac{d_{\text{fi}}}{\hbar} \right)^2 \frac{\sin^2\left[(\omega_{\text{fi}} - \omega)t/2\right]}{(\omega_{\text{fi}} - \omega)^2}. \tag{1.15}$$

In the resonant case $\omega = \omega_{\text{fi}}$, the probability of transition increases quadratically with time

$$P_{\text{fi}}(t) = \frac{1}{4} \left(\frac{d_{\text{fi}}}{\hbar} \right)^2 t^2. \tag{1.16}$$

For ω different from ω_{fi}, the probability of transition oscillates in time. Therefore, resonant transition dominates. [Schinke, 1993, Loudon, 1983]

We can rewrite Equation 1.15 assuming long duration of perturbation using the Dirac delta-function representation

$$\delta(\omega_{\text{fi}} - \omega) = \frac{2}{\pi} \lim_{t \to \infty} \frac{\sin^2\left[(\omega_{\text{fi}} - \omega)t/2\right]}{(\omega_{\text{fi}} - \omega)^2 t} \tag{1.17}$$

as

$$P_{\mathrm{fi}}(t) = \frac{\pi}{2}\left(\frac{d_{\mathrm{fi}}}{\hbar}\right)^2 t\,\delta(\omega_{\mathrm{fi}} - \omega). \tag{1.18}$$

This expression represents the probability of a transition from the initial to the final state by time t. The transition rate is constant in time:

$$k_{\mathrm{fi}} = \frac{\mathrm{d}}{\mathrm{d}t}P_{\mathrm{fi}}(t) = \frac{\pi}{2}\left(\frac{d_{\mathrm{fi}}}{\hbar}\right)^2 \delta(\omega_{\mathrm{fi}} - \omega). \tag{1.19}$$

This transition rate can be used to derive a formula for absorption cross section $\sigma(\omega)$. Imagine a beam of monochromatic light with resonant frequency $\omega = \omega_{\mathrm{fi}}$ propagating through a cavity of volume V, and containing a gas of N particles. Let us now consider a slice perpendicular to the axis of the beam propagation (for example z-axis) with area A and length $\mathrm{d}z$, which is so thin we can assume the energy density W being constant inside. Then the energy of the beam of light inside the slice is

$$S = A\,\mathrm{d}z\,W \tag{1.20}$$

and decreases within a time interval $\mathrm{d}t$ due to the absorption by

$$\mathrm{d}S = -n\,\hbar\,\omega_{\mathrm{fi}}\,k_{\mathrm{fi}}\,\mathrm{d}t, \tag{1.21}$$

where $n = NA\mathrm{d}z/V$ is the number of particles inside the slice and $\hbar\omega_{\mathrm{fi}}$ represents the energy absorbed by one particle. Combination of Equations 1.21, 1.20 and 1.19 and the definition of $d_{\mathrm{fi}} = \langle\Psi_{\mathrm{f}}| - \hat{\mathbf{d}}\cdot\mathbf{E}_0|\Psi_{\mathrm{i}}\rangle$ used in Equation 1.10 leads to the equation

$$\mathrm{d}W = \mathrm{d}S/(A\mathrm{d}z) = -\omega_{\mathrm{fi}}\,\delta(\omega_{\mathrm{fi}} - \omega)\,\mathrm{d}t\,\frac{\pi N}{2\hbar V}\,\left|\langle\Psi_{\mathrm{f}}| - \hat{\mathbf{d}}\cdot\mathbf{E}_0|\Psi_{\mathrm{i}}\rangle\right|^2. \tag{1.22}$$

Expressing $\mathbf{E}_0$ as $\mathbf{E}_0 = E_0\,\mathbf{e}$, where $\mathbf{e}$ is the unit vector in the direction of electric field and E_0 its amplitude, and using the relation $E_0^2 = 2W/\epsilon_0$, where ϵ_0 is the electric permitivity, we can rewrite Equation 1.22 as

$$\frac{\mathrm{d}W}{\mathrm{d}t} = -\omega_{\mathrm{fi}}\,\delta(\omega_{\mathrm{fi}} - \omega)\,\frac{\pi N W}{\hbar\epsilon_0 V}\,\left|\langle\Psi_{\mathrm{f}}| - \hat{\mathbf{d}}\cdot\mathbf{e}|\Psi_{\mathrm{i}}\rangle\right|^2. \tag{1.23}$$

In order to determine $\sigma(\omega)$, we will now use the Lambert–Beer law describing the intensity decrease during the beam propagation in z-direction

$$I(z) = I_0\,e^{-\sigma\rho z} \tag{1.24}$$

or

$$\frac{\mathrm{d}I(z)}{\mathrm{d}z} = -\sigma(\omega)\rho I, \tag{1.25}$$

where ρ is the density of the gas in cavity $\rho = N/V$. The last equation can be connected to Equation 1.23 via the relations $\mathrm{d}W/\mathrm{d}t = \mathrm{d}I/\mathrm{d}z$ and $W = I/c$, where c is the speed of light. Therefore, for the absorption cross section we get

$$\sigma(\omega) = \frac{\pi}{\hbar\epsilon_0 c}\,\omega_{\mathrm{fi}}\,\delta(\omega_{\mathrm{fi}} - \omega)\,\left|\langle\Psi_{\mathrm{f}}| - \hat{\mathbf{d}}\cdot\mathbf{e}|\Psi_{\mathrm{i}}\rangle\right|^2. \tag{1.26}$$

The absorption cross section has the units of area. [Schinke, 1993, Loudon, 1983]

Now we will employ the Born-Oppenheimer approximation [Schinke, 1993], which means we will separate the nuclear motion from the motion of electrons (heavy nuclei move infinitely slowly compared with electrons). For the various states, the time-independent molecular wavefunction within this approximation is

$$\mathit{\Psi}_{kl}(\mathbf{Q},\mathbf{q}) = \varphi^{\mathrm{nu}}_{kl}(\mathbf{Q})\,\mathit{\Xi}^{\mathrm{el}}_{k}(\mathbf{q};\mathbf{Q}), \tag{1.27}$$

where $\mathit{\Xi}^{\mathrm{el}}_{k}(\mathbf{q};\mathbf{Q})$ is the kth solution of the electronic Schrödinger equation and $\varphi^{\mathrm{nu}}_{kl}(\mathbf{Q})$ is the lth solution of the nuclear Schrödinger equation for the kth electronic state. The absorption cross section $\sigma(\omega)$ within the Born-Oppenheimer approximation is

$$\begin{aligned}\sigma(\omega) = \frac{\pi}{\hbar\epsilon_0 c}\,&\omega_{k_f l_f,k_i l_i}\,\delta(\omega_{\mathrm{k_f l_f,k_i l_i}} - \omega)\\ &\times\left|\langle\varphi^{\mathrm{nu}}_{k_f l_f}(\mathbf{Q})| - \mathbf{e}\cdot\boldsymbol{\mu}_{k_f k_i}(\mathbf{Q})|\varphi^{\mathrm{nu}}_{k_i l_i}(\mathbf{Q})\rangle\right|^2,\end{aligned} \tag{1.28}$$

in which we defined the transition dipole moment as[1]

$$\boldsymbol{\mu}_{k_f k_i}(\mathbf{Q}) = \langle\mathit{\Xi}^{\mathrm{el}}_{k_f}(\mathbf{q};\mathbf{Q})\,|\,\hat{\mathbf{d}}\,|\,\mathit{\Xi}^{\mathrm{el}}_{k_i}(\mathbf{q};\mathbf{Q})\rangle\,. \tag{1.29}$$

Under the ideal conditions, the absorption cross section is a series of discrete lines with different amplitudes. In reality, these conditions are never achieved due to various reasons (e.g. non-monochromatic light, finite pulse duration or energy level broadening), i.e. the lines are broadened. [Schinke, 1993]

The theory derived in this chapter assumed bound-bound transitions, but it is possible to extend it to bound-free transitions (dissociation), as discussed in more detail in Schinke [1993]. In the case of bound-free transitions, the absorption cross section line broadening caused by dissociation generally exceeds the broadening caused by other effects.

1.4 $\mathbf{E}_0$-$\boldsymbol{\mu}$-v vector correlation in photodissociation dynamics

In Chapter 1.2.1 we discussed the scalar properties of the products of photodissociation – the energy distribution. However, photodissociation is a vector process (assuming application of a polarized light), and thus the angular distribution of the photoproducts is substantial for the complete understanding of the whole dynamics.

Let us consider three vectors: the polarization vector of the dissociation light $\mathbf{E}_0$, the transition dipole moment of the parent molecule $\boldsymbol{\mu}$ and the recoil velocity of the photofragment $\mathbf{v}$. Vectors $\boldsymbol{\mu}$ and $\mathbf{v}$ are aligned with respect to $\mathbf{E}_0$, which defines a direction in the laboratory frame. In the previous chapter, we derived the formula for the probability of the absorption of photon, which depends on the mutual alignment of vectors $\mathbf{E}_0$ and $\boldsymbol{\mu}$, and is proportional to $\cos(\alpha)$, where α is the angle between $\mathbf{E}_0$ and $\boldsymbol{\mu}$. Considering a diatomic molecule, the transition

---

[1] Integration over all electronic coordinates.

dipole moment $\boldsymbol{\mu}$ can be either parallel or perpendicular to the molecular bond. The molecular dissociation rates are in most cases much higher than the rotation rates, thus, the recoil velocity $\mathbf{v}$ of the fragment is always either perpendicular or parallel to the transition dipole moment, because the fragment flies away in the direction of the bond (see Figure 1.3). Fixed angular correlation between vectors $\boldsymbol{\mu}$ and $\mathbf{v}$ leads to the angular correlation between $\mathbf{v}$ and $\mathbf{E}_0$. This was first pointed out by Zare and Herschbach [1963], who derived the equation for normalized angular distribution of photodissociation products

$$I(\theta) = \frac{1}{4\pi}\left[1 + \beta P_2(\cos\theta)\right], \tag{1.30}$$

where θ is the angle between $\mathbf{E}_0$ and $\mathbf{v}$, β is the anisotropy parameter and P_2 is the second-order Legendre polynomial

$$P_2(x) = \frac{3x^2 - 1}{2}. \tag{1.31}$$

This equation can be used for single photon processes. [Houston, 1987, Schinke, 1993]

The values of anisotropy parameter β are ranging from -1 to 2. In Figure 1.3, three cases are illustrated. For $\beta = -1$, the transition is perpendicular, as can be seen in the left part of Figure 1.3, $\beta = 0$ corresponds to the spatially isotropic transition as depicted in the middle, and finally, $\beta = +2$ corresponds to the parallel transition (right part of Figure 1.3). By measuring the angular distribution of the photofragments and determining the parameter β, we obtain information about the nature of the electronic transition (and thus the excited state). [Houston, 1987, Schinke, 1993, Fárník, 2011]

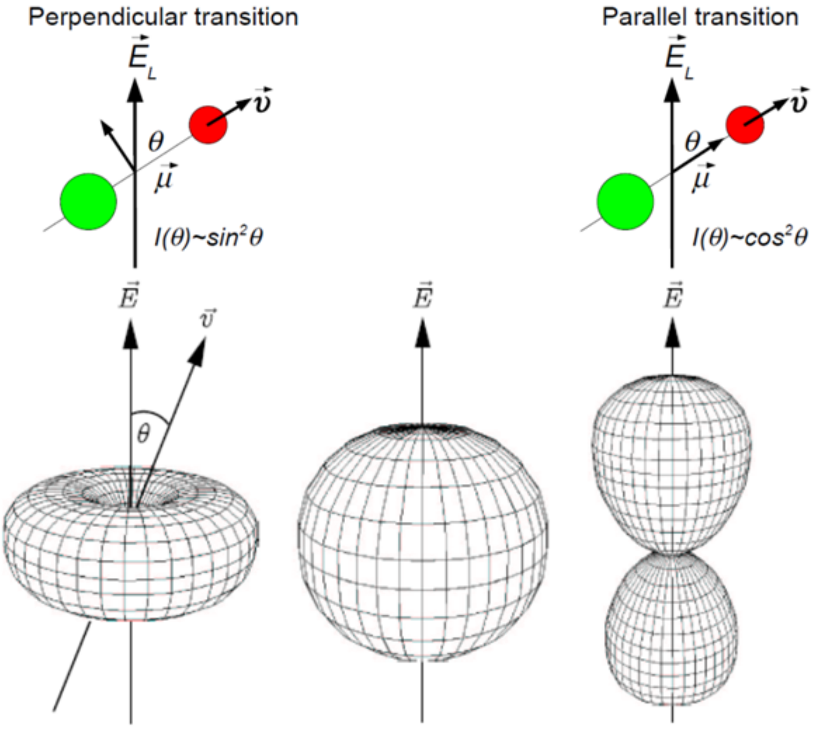

Figure 1.3: Angular distribution of the photodissciation process, which is anisotropic. Here, $\mathbf{E}_0$ is denoted $\mathbf{E}_L$. Image taken from Fárník [2011].

2. Experiment

2.1 Molecular beams

It was in 1911 when Dunnoyer first produced the molecular beam and demonstrated that atoms inside a vacuum chamber move along straight lines without mutual interactions. During the 20th century, this technique developed and molecular beams became one of the most important research tools for both physics and chemistry. The discovery of molecular beams contributed, among other things, to the experimental proof of the kinetic theory of gases or to the development of quantum mechanics (namely in Stern–Gerlach experiment, which showed that the spatial orientation of angular momentum is quantized). Thanks to molecular beams, chemists could observe the mechanism and dynamics of the fundamental chemical processes for the first time. Another area of interest are cluster beams, as clusters represents the transition between a single atom (or molecule) and bulk, and have unique properties. With the continuing technological progress, molecular beams did not become an outdated research method. On the contrary, they are still bringing new impulses and challenges for both the basic research and applications. [Pauly, 2000]

Molecular beams are also an interesting tool in terms of atmospheric chemistry, because thanks to them we can imitate atmospheric processes in laboratory conditions.

2.1.1 Supersonic expansion

The source of the molecular beam may be a container with gas in thermal equilibrium, from which the gas molecules escape through a nozzle into a vacuum. In principle, such a beam source can be divided into two types characterized by the Knudsen number K_n [Pauly, 2000]

$$K_{\mathrm{n}} = \frac{\lambda}{d}, \tag{2.1}$$

where λ is the mean free path of the molecules in the container and d denotes the typical nozzle dimension, e.g. diameter.

If $K_{\mathrm{n}} > 1$, the source is effusive. The dimension of the nozzle d is smaller than the mean free path of the molecules λ inside the container, and thus there are not many collisions in the immediate vicinity of the nozzle. The molecules leaving the container are actually those that entered the hole in the wall. Hence, the resulting effusive molecular beam can be described using the kinetic theory of gases. The Maxwell-Boltzmann velocity distribution of the molecules is roughly maintained, the beam has a cosine-angular distribution and relatively low intensity. [Vallance, 2017]

Although the effusive beams are historically older and were used first, today they are used for special applications. More interesting and relevant to this thesis is the second type of the molecular beam source – the supersonic source. For this source, the condition $K_{\mathrm{n}} \ll 1$ applies, which means that the mean free path of the molecules λ is much smaller than the nozzle dimension d, thus, many collisions occur during the passage of the molecules through the nozzle. We no longer observe the exit of individual molecules into the vacuum, but the expansion of a fluid in which the molecules are in mutual interaction with each other. The pressure difference is accelerating the gas out of the container, and for the pressure difference large enough, the gas flow at the nozzle throat reaches the local speed of sound and is underexpanded. Thus, it continues its expansion in the region behind the nozzle and reaches supersonic speeds. The local speed of sound is lower in the region behind the nozzle than in the container, as the gas is cooling down during the expansion. [Pauly, 2000]

The large number of collisions of molecules guarantees a local equilibrium at each point along the expansion, which can be considered adiabatic (collisions between molecules predominate over collisions of molecules with the wall). Behind the nozzle, the gas density gradually decreases and the number of collisions of molecules in the beam is therefore reduced. This means that changes in flow properties no longer occur at distances larger than the mean free path of molecules, and the local equilibrium that we can consider at the beginning of expansion is no longer ensured from a certain point. Relaxation processes slow down due to reduced collision rate and eventually stop. All that lead to the non-equilibrium transition, which occurs in the area called the quitting or the sudden freeze surface. This surface divides the expansion into two parts: the isentropic flow of the continuous medium and the flow of free molecules without mutual collisions. [Pauly, 2000, Fárník and Lengyel, 2017]

The total number of collisions that one molecule experiences during the expansion is in the order of 10^2 to 10^4. Kinetic processes which require a similar or smaller amount of collisions will equilibrate with other degrees of freedom during the expansion. For example, the rotation of diatomic molecules usually require only 10–100 collisions to achieve equilibrium with the translational degree of freedom. Therefore, rotational modes transfer their energy into the beam flow and reach their terminal state before the quitting surface. However, vibrational cooling is not that efficient, and thus the vibrational modes freeze at the quitting surface before reaching their terminal state since there are not enough collisions. Hence, during the supersonic expansion, vibrational states of the molecules often remain unchanged. Due to the non-equilibrium transition, the translational, rotational and vibrational temperature might not reach equilibrium and each has a different value. [Pauly, 2000]

During collisions, molecules have converted their random translational energy and enthalpy into kinetic energy along the direction of beam propagation. Unlike the effusive beam, the speed distribution of molecules inside the supersonic beam is very narrow, which means that the temperature of the gas (determined by the speed distribution width) is extremely cold. The angular distribution is also much narrower compared with the effusive beam. [Vallance, 2017]

For now, let us consider that all the enthalpy of the molecules is converted into the kinetic energy of the molecular jet. In this way we can calculate the terminal velocity u_∞ of the molecules inside the beam propagating along the x-axis, as described in Fárník [2011]. The total energy e of a unit element of an expanding gas of a mass m is the sum of its enthalpy h and the kinetic energy:

$$e(x) = h(x) + \frac{mu^2(x)}{2}. \tag{2.2}$$

This energy must be conserved along the x-axis. As the molecule velocity inside the container is not directed (i.e. the directed velocity u_0 equals zero), for the enthalpy of the unit element in the source h_0 applies

$$h_0 = h(x) + \frac{mu^2(x)}{2}. \tag{2.3}$$

For an ideal gas we can write

$$h_0 - h(x) = \int_T^{T_0} \frac{c_\mathrm{p}}{N_\mathrm{A}} \,\mathrm{d}T' = \frac{c_\mathrm{p}(T_0 - T)}{N_\mathrm{A}}, \tag{2.4}$$

where N_A denotes the Avogadro constant, c_p is the molar heat capacity at a constant pressure, which we assume to be temperature independent, T_0 is the temperature of gas in the container and $T = T(x)$ is the temperature of expanding gas at given point x. The molar heat capacity c_p can be expressed as

$$c_\mathrm{p} = N_\mathrm{A} k_\mathrm{B} \frac{\gamma}{\gamma - 1}, \tag{2.5}$$

where k_B is the Boltzmann constant and γ is the heat capacity ratio defined as $\gamma = c_\mathrm{p}/c_\mathrm{V}$, where c_V is the molar heat capacity at a constant volume. Under our assumption that all the internal energy is transformed into kinetic energy, the terminal temperature must be $T = T_\infty = 0$. For the final velocity, following formula can be derived using the equations above

$$u_\infty = \sqrt{\frac{2k_\mathrm{B}T_0}{m} \frac{\gamma}{\gamma - 1}}. \tag{2.6}$$

It might seem that the terminal speed is the upper limit for the speed of the molecular beam, however, that is not true. During the clustering process the condensation energy is released, allowing the beam particles to reach even higher speeds than u_∞ [Fárník, 2011]. It can be noticed that the terminal velocity u_∞ is not much higher than the most probable velocity of the molecules in the container (following Maxwell-Boltzmann distribution), which is $u_\mathrm{MB} = \sqrt{\frac{2k_\mathrm{B}T_0}{m}}$.

In point of fact, some of the thermal velocity $\alpha = \sqrt{\frac{2k_\mathrm{B}T}{m}}$ is being maintained by the molecules, however, it is typically one or two orders of magnitude smaller than the directed beam velocity. The quality of the expansion, which is in fact the efficiency of molecular cooling, can be expressed as a speed ratio

$$S = \frac{u}{\alpha} \approx 2\sqrt{\ln 2}\frac{u_\mathrm{e}}{\mathit{\Delta} u_\mathrm{e}}, \tag{2.7}$$

where u_e is the velocity of the molecules (determined experimentally) and $\mathit{\Delta} u_\mathrm{e}$ denotes the the measured velocity distribution's full width at half maximum (FWHM), which corresponds to the random (thermal) velocity. [Fárník, 2011]

The supersonic speed of the jet behind the nozzle throat leads to a barrel-shaped shock wave, which surrounds the so-called zone of silence, where the molecular beam does not feel any turbulences caused by the shock wave. Using a skimmer of a suitable shape placed before the Mach disk, it is possible to extract the beam from this zone into another differentially pumped chamber. There we have a molecular beam full of cool isolated molecules (or clusters) ready for the experiments. [Fárník, 2011]

2.1.2 Cluster formation

Molecular and cluster beams are closely related. The apparatus for their generation is essentially the same – the degree of clustering of molecules may be affected by changing the experimental conditions and the geometry of the source.

With decreasing expansion temperature, the interaction time between the molecules is increasing, which leads to cluster formation [Fárník, 2011]. The starting point for clustering are dimers, which are formed mainly during the three body collisions and serve as a condensation nuclei for further growth. The theoretical description of cluster growth is very complicated and there is no generally valid rigorous theory. In practice, however, semiempirical scaling laws are often sufficient. [Pauly, 2000]

The cluster size, together with other parameters such as cluster temperature or internal energy, freezes in the quitting surface area and no longer changes. The quitting surface is typically located at a distance of 20 times the nozzle diameter behind the nozzle. Thus, for a nozzle with a diameter of 100 μm, quitting surface is only 2 mm away from the nozzle throat, and therefore the clustering and nucleation process in supersonic expansions is difficult to investigate [Pauly, 2000, Fárník and Lengyel, 2017]. However, there are also experiments with macroscopic nozzles (e.g. Laval nozzle), in which the nucleation process is directly investigated in the supersonic expansion [Chakrabarty et al., 2017, Ferreiro et al., 2016].

As a consequence of the mass and heat exchange kinetics, the clusters have a higher internal temperature during the condensation process compared with the surrounding gas. Upon the growth completion, their temperature drops sharply, mainly due to the evaporation [Pauly, 2000]. The internal temperature of clusters formed during supersonic expansion is very difficult to measure experimentally. In principle, it is only possible in some special cases. One of the examples can be a rotational-vibrational spectroscopy of the molecule embedded in the cluster. This method works for superfluid helium clusters, which allow the embedded molecules to move freely, making it possible to determine the rotation temperature [Toennies and Vilesov, 2004]. However, for most clusters, we can only estimate the temperature using the model approaches [Fárník and Lengyel, 2017].

Clusters prepared in supersonic molecular beams have a certain size distribution. For small clusters, we observe that the size distribution decreases exponentially from monomers to larger clusters. When generating rather larger clusters, the size distribution is typically described by the log-normal distribution. [Fárník and Lengyel, 2017]

The cluster size distribution can be obtained relatively easily, for example, with the help of mass spectrometry (described later in this chapter). However, this method requires cluster ionization, which can lead to strong fragmentation because the clusters are weakly bound. Therefore, we are losing information about the original size of the neutral clusters. The accurate cluster size determination in the beam still remains a challenge. The mean cluster size $\bar{N}$ (i.e. the mean number of atoms or molecules in the cluster) can be estimated using semiempirical laws. For example, for rare gases, the clustering process can be described using a dimensionless Hagena's scaling parameter Γ^*, on the basis of which we can determine the mean size $\bar{N}$. This size is dependent, among others, on the stagnation pressure, temperature and nozzle shape. Therefore, by setting external parameters, the mean cluster size can be affected. Exact formulas can be found for example in Fárník and Lengyel [2017] or Buck and Krohne [1996]. Hagena's scaling parameter was adjusted for ammonia (NH_3) and water clusters (H_2O). These clusters are often of interest because of their atmospheric and astrochemical relevance. For details see Bobbert et al. [2002].

Clusters are often generated in so-called seeded expansions, where small concentrations (less than 10%) of the investigated molecules are added to the expansion of a carrier gas (typically a rare inert gas such as helium or argon). The heavy molecules co-expand with the rare gas carrier, in which they are embedded, and the beam velocity for such expansions is mostly determined by the carrier gas. Heavy molecules co-expanded in small concentrations with helium typically reach higher speeds due to helium's small mass. Helium is light and does not interact with embedded molecules, and thus does not support clustering. Therefore, it is suitable for monomer research. Heavier argon, in contrast, makes clustering of embedded molecules efficient and support the production of larger clusters. However, these clusters are often not pure because the interaction between argon and other molecules is stronger than that of helium. [Fárník, 2011]

It is also possible to create clusters with adsorbed molecules of another species on the surface. Such mixed clusters can be prepared in following way: first, we generate required clusters in the molecular beam by standard method, second, we let the beam pass through one or several pick-up chambers with variable pressure, in which the molecules of another species can be adsorbed (picked-up) on the clusters surfaces. Depending on the nature of intermolecular interactions, the picked-up molecules may either penetrate into the cluster or remain on its surface, where they may eventually coagulate and form small clusters. [Fárník, 2011]

Molecular beam experiments are carried out in evacuated chambers and have large demands on the pumping speed requirements. To minimize such requirements, pulsed expansion can be used. Than, the timing of the experiment is crucial, as the valve opening and closing is changing the pressure and temperature, and affecting the expansion. [Fárník and Lengyel, 2017]

2.2 Velocity map imaging

2.2.1 TOF spectrum of photodissociation fragments

The energetics and the angular distribution of the molecule fragments after photodissociation has been already described in Chapter 1.2. How can we access the information about photodissociation dynamics experimentally? We can use the time-of-flight (TOF) spectrometer.

Let us begin with the general description of the TOF as a mass spectrometers. The mass spectrometers are an indispensable analytical tool for many scientific disciplines. Thanks to them we can identify a chemical compound based on the molecular and atomic masses of its components. The mass spectrometers operate under a high vacuum and consist of three parts: ion source, analyzer and detector. The ions generated in the ion source are extracted and than divided in the field-free analyzer according to the mass-to-charge ratio m/z. After that they are captured by the detector. To make the reading of the mass spectra as straightforward as possible, the mass-to-charge ratio is defined as dimensionless ratio of the ionic mass m in the unified atomic mass units (u) and the number of elementary charges of the respective ion (z). For $z = 1$, the ratio m/z directly corresponds to the relative molecular (or atomic) mass of the measured ion. The unified atomic mass unit has been defined since 1961 as the 1/12 of the rest mass of the atom ^{12}C in the ground state, whose atomic mass is thus precisely defined as 12 u. [Gross, 2011]

A mass spectrum is an intensity versus m/z plot representing the chemical analysis of the ionized sample. The position of the peak corresponds to the m/z of the ion that was generated in the ion source. The intensity of the peak correlates with the measured abundance of a particular ion. It should be mentioned that from each ionized cluster we obtain one ion only, thus, for the spectrum to have a statistical value, it is necessary to collect information about thousands of ion fragments. Also, to properly interpret the mass spectra, it is necessary to take into account the different masses of the individual isotopes of each element and their relative amounts. Each element is determined by the number of protons in its nucleus, which indicates the atomic number Z. Atoms with the same atomic number, which differ only in the number of neutrons in the nucleus, are called isotopes. [Gross, 2011]

An important part of mass spectrometers is the analyzer, which separates ions according to m/z. The analyzer relevant to this thesis is the one operating on the TOF principle. That means we are measuring how much time it takes the ions to reach the detector.

After ionization, the ion cloud is accelerated by the electric field. For simplicity, let us now assume that all ions are accelerated at the same time, from the same point, and initially have zero velocity. In the ion source, which is also extractor, the ions gain energy

$$E_{el} = ez\mathit{\Delta} U = \frac{1}{2} m_i v^2 = E_{kin}, \tag{2.8}$$

where e is the electron charge, z number of ion charges, $\mathit{\Delta} U$ is the potential difference between two electrodes (repeller and extractor), m_i is the mass of the ion and v is the ion speed obtained during acceleration. Ions are extracted into the field-free region of analyzer of length l, where they are separated due to different mass-to-charge ratios, and thus different speeds:

$$v = \sqrt{\frac{2ze\mathit{\Delta} U}{m_i}}. \tag{2.9}$$

The formula for the time of flight τ can be easily derived using the simple relation $\tau = l/v$:

$$\tau = \frac{l}{\sqrt{2e\mathit{\Delta} U}} \sqrt{\frac{m_i}{z}}. \tag{2.10}$$

We can see that lighter ions reach the detector faster. [Gross, 2011]

There are many ways how to ionize particles in the ion source. We will focus on the resonance-enhanced multiphoton ionization (REMPI), described in more detail in Chapter 2.2.3, which is very effective and allows us to selectively choose the desired particles only.

Now let us go back to the photodissociation experiment. TOF principle can be used not only to measure mass spectra but also to measure the energy released during the photodissociation process. Particles in the molecular beam are dissociated and then the selected fragments are ionized inside the intersection (or extraction) region between two electrodes: repeller and extractor. Again, the electric field between these two electrodes accelerates the ionized fragments towards the field-free region of the length l at the end of which is the detector. The parent molecules are randomly oriented in the extraction region, which means that after dissociation the ionized fragments gain recoil velocity $\vec{u}$ (from the excess energy) pointing in different directions, depending on the original direction of the broken bond. Let us have a look at two oppositely oriented molecules of the same specie as depicted in Figure 2.1. After photodissociation and selective ionization, each of the extracted fragment will reach the detector at a different time, even though they have the same mass. That is due to the fact they have the recoil velocities $\vec{u}$ in the opposite directions. This time difference is called turn around time $\varDelta\tau$ and carries information about the initial velocity of the fragment obtained after the photodissociation, and thus about the energy distribution. The time-of-flights of the molecules' fragments are

$$\tau_{1,2} = \frac{l}{v \pm u}. \tag{2.11}$$

The turn around time $\varDelta\tau$ can be calculated as

$$\varDelta\tau = \tau_1 - \tau_2 = \frac{2lu}{v^2 - u^2} \approx \frac{2lu}{v^2}, \tag{2.12}$$

where we used the aproximation $v^2 \gg u^2$. Substituting for v (Equation 2.9), we get the final relation for the turn around time

$$\varDelta\tau = \frac{lm}{ze\varDelta U}u. \tag{2.13}$$

We can see that the turn around time depends on the recoil speed of the fragment obtained after the photodissociation, and thus carries information about the energy distribution of the broken parent molecule. [Fárník, 2020, Whitaker, 2003]

In fact, the ions are not accelerated from one point in the extractor. They have a certain spatial distribution. This leads to the broadening of the peak lines of the mass spectra, and thus affect the resolution of the spectrometer. Such problem can be overcomed by using a two-stage ion source proposed by Wiley and McLaren [1955] (and discussed for example in Boesl [2016]). By adding the third electrode (liner), the initial spatial distribution of ions is compensated. At a certain point, the ions of same masses meet. That is where we place the detector and measure narrow peaks.

It can be shown that the space focusing conditions depend on the ratio of the potential difference between repeller and extractor electrode and the potential difference between extractor and liner electrode. It does not depend on the concrete values of individual potential differences. Thanks to this, the TOF spectrometer can operate in two modes – high-field and low-field mode. Working in high-field mode, we can neglect the the initial kinetic energies, which the fragment ions attain in the fragmentation process after the ionization, and measure

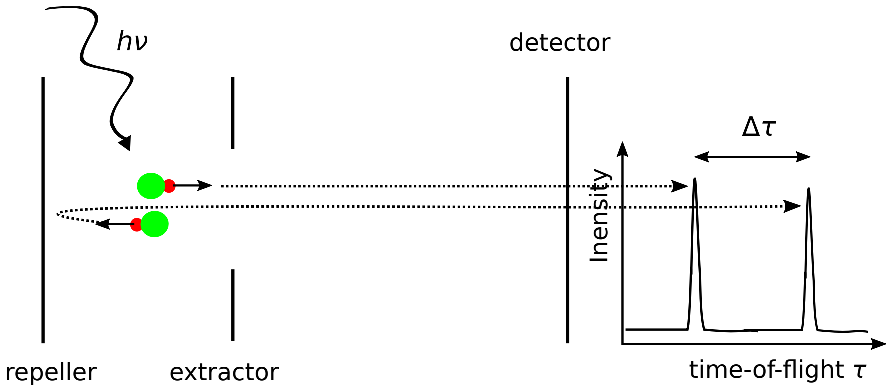

Figure 2.1: Photodissociation of two identical molecules with opposite respective alignment. After the fragment ionization, the intensity versus time-of-flight plot shows two peaks due to the different initial velocities of the measured fragments. The kinetic energy of the fragment after the dissociation can be calculated from the turn around time $\Delta\tau$.

the TOF mass spectra. Working in low-field mode, the initial kinetic energies cannot be neglected. Mass spectrometer changes into the energy analyzer and we measure two (or more, depending on the number of dissociative states) narrow peaks corresponding to the original speed and direction of the fragments after photodissociation.

There is a significant obstacle when measuring the TOF spectra of photodissociation fragments. Dissociated fragments depart in many different directions. Fragments with the recoil velocity $\vec{u}$ in the direction oblique to the axis perpendicular to the detector hit the detector sooner or later depending on their velocity projection into this axis. We are not measuring the sharp peaks, but their profile as illustrated in Figure 2.2. In order to achieve the best possible resolution, and to be able to deduct $\Delta\tau$, we can filter out fragments pointing obliquely using a slit. Then our measured data have good resolution, but the signal is low as most of the fragments are being filtered out. Another inconvenience is that when measuring fragments departing in one direction only, we are not obtaining the full information about the angular distribution. The angular distribution depends on the polarization of the photodissociation laser, so we can perform a set of measurements with differently aligned polarization to obtain the angular distribution, however, this significantly extends the measurement time.

2.2.2 Further development

The ion imaging method bypasses the problems arising in the TOF spectrometer and is more suitable for the photodissociation experiment. The main innovation, proposed by Chandler and Houston [1987], is the position-sensitive detector which is large enough to pick up the ionized fragments with different recoil velocities $\vec{u}$. The detector consists of a pair of micro-channel plates (MCPs) behind which

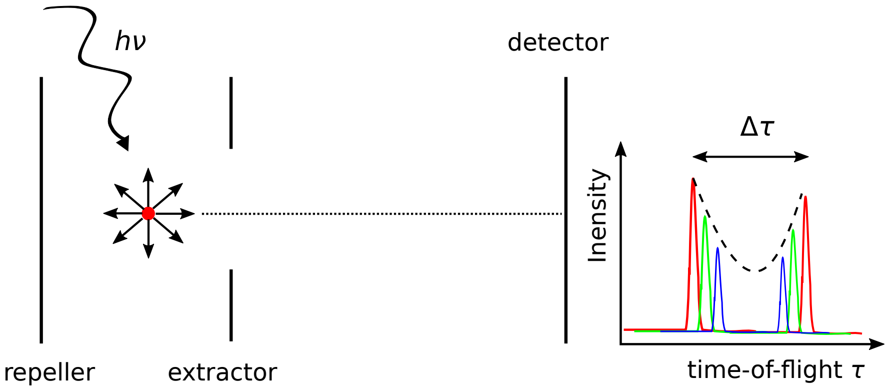

Figure 2.2: Ionized fragments have different directions of the initial velocities due to different alignment of the parent molecules. This is reflected in the measured TOF spectrum.

is a phosphor screen. When the ion hits the MCP, an avalanche of electrons from one of MCP's channels emerges onto the phosphor screen, producing a flash which is than recorded by a CCD (charge-coupled device) camera. Thus, we know where each individual ion fragment landed spatially and integrating image over some time period, gradually, we obtain the image, which is the projection of the initial velocities $\vec{u}$ of the fragments onto the plane of the detector. From this image it is possible to determine the 3D spatial distribution of the state-selected photofragments. The problem of ion imaging technique was that the grid electrodes in the arrangement according to Wiley and McLaren caused blurring of the image. Later improvement of Eppink and Parker [1997] solved this problem and the method of ion imaging was named the velocity map imaging (VMI). Eppink and Parker exchanged grid electrodes with electrostatic lenses tuned so that ionized fragments of the same velocity vector $\vec{u}$ hit the same point (channel) of the MCP detector, regardless of their initial spatial position.

Let us now consider a photodissociation process generating fragments that are leaving the interaction region in all directions. The fragments of the same specie form a so-called Newton's sphere. After selective ionization, the expanding Newton's sphere is being accelerated towards the detector. The electric field of the ion optics is tuned to compress the Newton's sphere for the selected ions along the time-of-flight axis creating a "pancake" which hits the detector simultaneously and forms a ring of radius corresponding to fragments' velocity. If the photodissociation results in different output pathways leading to the same fragments with different energetics, several rings of different radii may be recorded. In reality, photodissociation is an anisotropic process. Hence, incomplete rings, which contain the information about the nature of the electronic transition, are recorded (see Figure 1.3). From the VMI experiment we can simultaneously obtain information about both energy distribution and anisotropy, i.e., the nature of the excited state of the photoproducts. [Whitaker, 2003]

Finally, we add the last note. The speed distribution of state-selected photoproducts is not delta function. In principle, this means that image resolution will never be perfect (regardless of the imperfections of the experiment).

2.2.3 Resonance-enhanced multiphoton ionization

In our experiment, the lasers (described later) operate in a pump-probe scheme. First, the pump laser pulse initiates the reaction through the photodissociation of the molecules, and second, after a short delay, the probe laser pulse is used to state-selectively ionize some of the reaction products (i.e. photofragments). These selected ions are then extracted from the interaction region by ion optics towards the detector. For most molecules, single photon ionization is usually not feasible because soft X-ray photons, not accessible in most laboratories, would be needed. Furthermore, such ionization method would not be selective. Multiphoton ionization is also problematic. It is not selective and, in addition, it has low efficiency. Both these photoionization processes are schematically illustrated in Figure 2.3. In order to ionize the photofragments effectively and selectively, we make use of resonance-enhanced multiphoton ionization (REMPI). Selected photofragments first absorb m "state-matching" photons and are brought into an electronically excited intermediate state. Subsequent absorption of another n photons ionize the fragment. Described $(m + n)$ REMPI is a nonlinear process and requires intensities achievable in the laser focus. The ionization efficiency of a REMPI process is usually orders of magnitude higher than the ionization efficiency of a corresponding multiphoton non-resonant process. Provided that the intermediate excited state is energetically narrow, the resonant process can be achieved only at a specific wavelength and is thus highly selective – not only specie selective, but also quantum state selective. Thus, by REMPI we can ionize specifically certain specie (fragment) in a certain single quantum state. That is the biggest advantage of the REMPI process. For a given molecule, there are

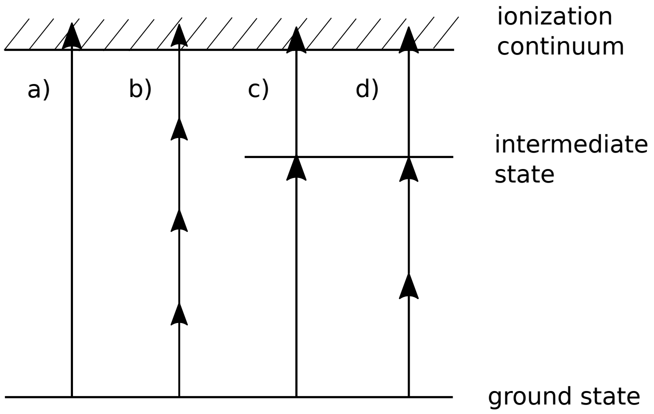

Figure 2.3: Photoionization scheme: a) single photon ionization, b) multi-photon non-resonant ionization, c) $(1 + 1')$ REMPI (the apostrophe indicates the use of a second laser of a different wavelength), d) $(2 + 1)$ REMPI.

usually several possibilities of different REMPI schemes that can be used. Two examples of REMPI are depicted in Figure 2.3. In practice, to reach the excited intermediate states of various atoms or molecules of various electronic states, we need a tunable laser. [Zimmermann and Hanley, 2021, Vallance, 2017]

2.2.4 Reconstruction methods

Although the recorded raw images provide some insight into the photodissociation dynamics, they are the projections of 3D Newton's spheres onto a 2D detector. In order to gain all the information about the photodissocition process, we need to reconstruct the original 3D velocity distribution. For the fragment distribution with an axis of cylindrical symmetry, inversion methods can be used to reconstruct the image. If the distributions lacks the symmetry, the forward convolution methods are needed, i.e. by optimizing parameters of a computer simulation one can try to reach the best agreement with the experimental data. [Whitaker, 2003]

In this chapter, one of the inversion methods, the **inverse Abel transformation**, will be described as it is the one that was used for the transformation of all our raw images. The polarization of the laser used for photodissociation in our experiment is parallel to the imaging plane of the detector. Thus, the velocity distribution of photofragments has cylindrical symmetry about an axis corresponding to the laser polarization vector (see Figure 1.3). Let us place the symmetry axis into the z axis of the Cartesian coordinate system with the origin in the point of the photodissociation. The velocity distribution of the ionized photofragments can be denoted as $i(x, y, z)$. If the ion cloud is extracted in the y-axis direction, the velocity distribution measured on the detector in the xz plane is

$$p(x, z) = \int_{-\infty}^{\infty} i(x, y, z)\,\mathrm{d}y. \tag{2.14}$$

Now we consider one row of the measured image along the x-axis at $z = z_0$, and denote the slice through the original 3D distribution $i(x, y; z_0) = s(x, y)$:

$$f(x) = p(x, z_0) = \int_{-\infty}^{\infty} s(x, y)\,\mathrm{d}y = 2\int_{0}^{\infty} s(x, y)\,\mathrm{d}y. \tag{2.15}$$

Thanks to the assumption that the function $s(x, y)$ is axially symmetrical, we can rewrite the last equation in polar coordinates introducing the substitution $r^2 = x^2 + y^2$:

$$f(x) = 2\int_{x}^{\infty} \frac{s(r)r}{\sqrt{r^2 - x^2}}\,\mathrm{d}r. \tag{2.16}$$

The above expression is called the Abel transform. To recover the original distribution $s(r)$, we need its inversion. How to obtain it can be found in Bracewell [2000]. The formula for the Abel transformation may be rewritten as

$$f(x) = \int_{0}^{\infty} k(r, x)s(r)\,\mathrm{d}r, \tag{2.17}$$

where

$$k(r, x) = \begin{cases} \frac{2r}{\sqrt{r^2 - x^2}}, & \text{if } |r| > |x|. \\ 0, & \text{if } |r| < |x|. \end{cases} \tag{2.18}$$

Changing the variables $\rho = r^2$, $\xi = x^2$, and letting $f(x) = F(x^2)$, $s(r) = S(r^2)$ we have

$$F(\xi) = \int_0^\infty K(\xi - \rho) S(\rho) \, \mathrm{d}\rho, \tag{2.19}$$

where

$$K(\xi - \rho) = \begin{cases} \frac{1}{\sqrt{\rho - \xi}}, & \text{if } \xi < \rho. \\ 0, & \text{if } \xi \geq \rho. \end{cases} \tag{2.20}$$

Equation 2.19 is a convolution integral, which can be also expressed as

$$F = K * S. \tag{2.21}$$

Applying the convolution theorem we can write

$$\hat{F} = \hat{K}\hat{S}, \tag{2.22}$$

where circumflex above the symbol of the function denotes the Fourier transform. Knowing that

$$\hat{K}(s) = \frac{1}{\sqrt{-2is}}, \tag{2.23}$$

we can express $\hat{S}$ as

$$\hat{S} = \sqrt{-2is}\hat{F} = -\frac{1}{\pi}\frac{1}{\sqrt{-2is}} i2\pi s \hat{F} = -\frac{1}{\pi}\hat{K}\widehat{F'}. \tag{2.24}$$

Therefore,

$$S = -\frac{1}{\pi} K * F', \tag{2.25}$$

which is

$$S(\rho) = -\frac{1}{\pi}\int_\rho^\infty \frac{F'}{\sqrt{\xi - \rho}} \, \mathrm{d}\xi. \tag{2.26}$$

Returning to the original variables yields

$$s(r) = -\frac{1}{\pi}\int_r^\infty \frac{\mathrm{d}f/\mathrm{d}x}{\sqrt{x^2 - r^2}} \, \mathrm{d}x. \tag{2.27}$$

This is, finally, the inverse Abel transformation that can be used to recover the original velocity distribution of the photofragment ions. We can apply the transformation to each row ($z = z_0$) of the image and reconstruct the original 3D ion distribution. Then we are interested in the sphere cross section in xz plane ($y = 0$). Unfortunately, there are some disadvantages related to this transformation due to the some degree of asymmetry that can arise because of the various effects during the measurement, and primarily due to the derivative in the integrand, which magnifies the noise. [Whitaker, 2003]

Several other reconstruction methods, and also slice imaging approach, an alternative experimental method which eliminates the need for inversion techniques, are described in Whitaker [2003].

From the inverted image, we can obtain the radial and angular distribution. To obtain the radial distribution, we need to summarize the intensities across a number of sample points, as our images are discrete set of pixels. Let us denote the intensity at a point (R, θ) of the image as $I(R, \theta)$, where R is the radial distance from the image centre, and θ is the angle between the z-axis (defined by the laser polarization) and R-vector. The summarized radial distribution is [Whitaker, 2003]:

$$f(R) = \frac{1}{4R} \sum_{i=1}^{4R} I(R, \theta_i). \tag{2.28}$$

From the radial distribution, the kinetic energy distribution (KED) can be obtained, as described in Chapter 2.3.2.

To obtain the angular distribution, we need to sample a radial-angular segment between R_{min} and R_{max} (corresponding to the beginning and the end of the selected intensity ring in the transformed image) and $\theta - \varDelta\theta/2$ and $\theta + \varDelta\theta/2$ for each angle θ in selected range (usually full or half range) with step interval θ_{step}. The resulting distribution can be fitted with function $I(\theta) \approx \frac{1}{4\pi}\left[1 + \beta P_2(\cos\theta)\right]$ (Equation 1.30) to determine the anisotropy parameter $\beta(R)$. [Whitaker, 2003]

2.3 AIM

2.3.1 Description

Apparatus for IMaging (AIM), illustrated in Figure 2.4, is based on VMI technique, and used for the investigation of photodissociation dynamics.

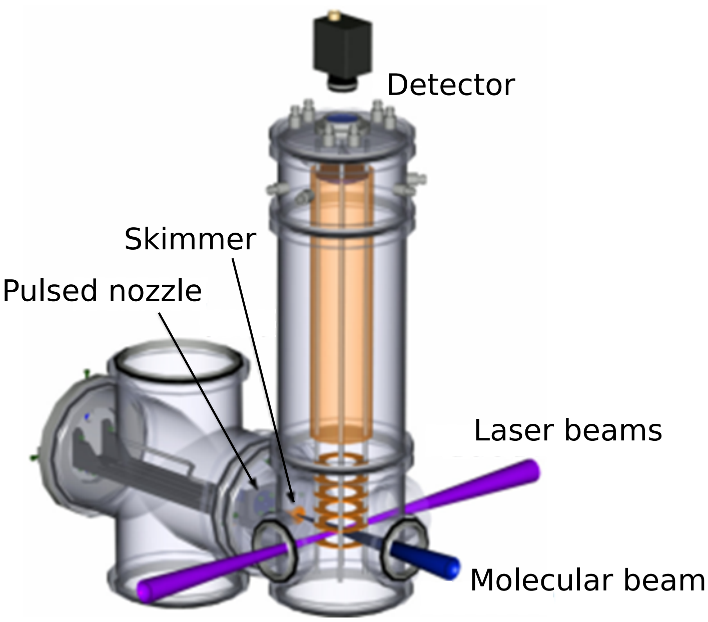

Figure 2.4: AIM scheme.

The apparatus consists of two chambers separated by skimer, and differentially pumped by turbomolecular vacuum pumps. The first chamber is the source chamber in which the molecular beam is formed during pulsed supersonic expansion. The second chamber is the interaction chamber, where the pulsed molecular beam is crossed with laser beams (usually two – one for photodissociation and other for REMPI) in the center of the chamber. The ionized photofragments are then analyzed using the VMI system, which is oriented perpendicularly to the molecular and laser beams. The ion optics, which are electrostatic lenses in an arrangement according to Eppink and Parker [1997], extracts the ionized photofragments generated in the intersection area towards the position sensitive detector.

Three electrodes provide the conditions for VMI: repeller on voltage $U_\mathrm{r} = 3.690\,\mathrm{kV}$, extractor on voltage $U_\mathrm{e} = 2.857\,\mathrm{kV}$ and ground. Voltage setting is sensitive on the position of the intersection region and is determined experimentally during calibration. Given values were used during the measurements for this thesis.

The detector consists of two MCPs in chevron stack coupled to a phosphor screen and followed by a CCD camera (controlled via a LabView program). The potential difference between front and back MCP accelerates the electrons created when an ion hits one of the channels. Electric pulses caused by the ions hitting the detector can be recorded and displayed on the oscilloscope. With the knowledge of time-of-flights, we obtain the TOF mass spectrum. The detector can be operated in two modes – continuous (front MCP is kept at zero potential and all ionic masses are detected) or gated (voltage pulse is applied on the front MCP so that the detector is activated only in the right time to record the ion of desired mass, thus, selectivity of the detection is increased). During our measurement of Cl fragments, the front MCP was gated with voltage between -0.25 and -0.35 kV and time duration 40 ns, whereas the back of MCP was kept at 1.15 kV.

The advantage of AIM is that the imaging chamber is close to the beam source. The intensity of the molecular beam decreases as $1/R^2$, where R is the distance from the source [Pauly, 2000]. The closer the imaging chamber is to the beam source, the higher signal is measured. Low signal means long measurement in order to obtain an image of statistical value. Another advantage of AIM is that thanks to pulsed beams we can generate and measure monomers. However, the expansion conditions in the pulsed beam change during the pulse duration and thus care must be taken to sample always the same point of the expansion. In addition, we cannot be completely sure if we generate clusters in the expansion or not, since the apparatus gives only very approximate results of the TOF mass spectra (it has been constructed primarily as the VMI analyzer and its performance as the TOF mass spectrometer is limited due to short analyzer length, low-field mode setting ect.). Another disadvantage of AIM is that we cannot measure complex mixed clusters (due to the absence of pick-up chambers).

2.3.2 Apparatus calibration

Before measuring, it is important to calibrate the apparatus and check the settings. Calibration is usually performed on HBr molecule due to its simple electronic structure, and due to the fact that we can use only one laser (of the wavelength 243.1 nm) for photodissociation of the molecule and also for the REMPI of the hydrogen fragment.

After the UV photon absorption, HBr molecule follows two dominant photofragmentation pathways:

$$\begin{aligned}\mathrm{HBr} + \hbar\omega \longrightarrow & \mathrm{H}(^2\mathrm{S}) + \mathrm{Br}(^2\mathrm{P}_{3/2}) \\ & \mathrm{H}(^2\mathrm{S}) + \mathrm{Br}^*(^2\mathrm{P}_{1/2})\end{aligned}$$

The photodissociation dynamics of HBr molecule is described for example in Smolin et al. [2006]. Briefly and simply, the molecule can be excited into several electronic states, some of them leading to the ground state products H and Br, the others leading to the ground state H and spin-orbit excited Br*. In the simplest case we can say that the former transition is perpendicular ($\beta = -1$) and the latter transition parallel ($\beta = +2$) for the excitation energy 5.1 eV (corresponding to the wavelength 243.1 nm).

Calibration proceeds as follows. First, the molecular beam is produced by expanding the mixture of HBr and buffer gas (He). Then, working in continuous mode, we try (iteratively) to align the beam, and find the best focusing conditions using the signal of parent ions HBr$^+$, which is narrow and intense.

After finding the ideal focusing conditions, it is also necessary to determine the orientation of the laser beam propagation relative to the CCD camera so that we can find the axis of symmetry. We achieve this by adjusting the voltage on the ion optics from VMI conditions to space focusing conditions.

Finally, we measure H photofragments image (gating mode is now on), transform them and acquire the radial distribution using the standard method described in previous chapter. Image and radial distribution of H photofragments can be found in Figure 2.5. After photodissociation, hydrogen fragments always exist in the ground state, but due to the fact their partners can exist in in the ground (Br) or exited (Br*) state, we can see two rings in the image. Now we need to determine the constant that converts the radial distribution in pixels to the KED in eV. The kinetic energy of the measured fragment is

$$E_{\mathrm{kin}} = \frac{1}{2}mu^2 = \frac{1}{2}m\frac{r^2}{\tau^2}, \tag{2.29}$$

where m and u are the fragment mass and recoil speed, respectively, and r is the path of the fragment (radius of the Newton's sphere). After the REMPI, ions are extracted into the analyzer of length l, and following applies to the time of flight of the fragment τ (for derivation of this formula see Chapter 2.2.1):

$$\tau = \frac{l}{\sqrt{2e\mathit{\Delta} U}}\sqrt{\frac{m}{z}}, \tag{2.30}$$

In the equation, e is the charge of the electron, z is the number of charges of the ion and $\mathit{\Delta}$U is the electric potential difference. Hence, the final equation for the kinetic energy of the ion is

$$E_{\mathrm{kin}} = \frac{ze\mathit{\Delta} U}{l^2}r^2 = K \cdot r^2. \tag{2.31}$$

In order to finish the calibration, we need to identify the constant K. By fitting the faster peak in the radial distribution (Figure 2.5), we can determine r

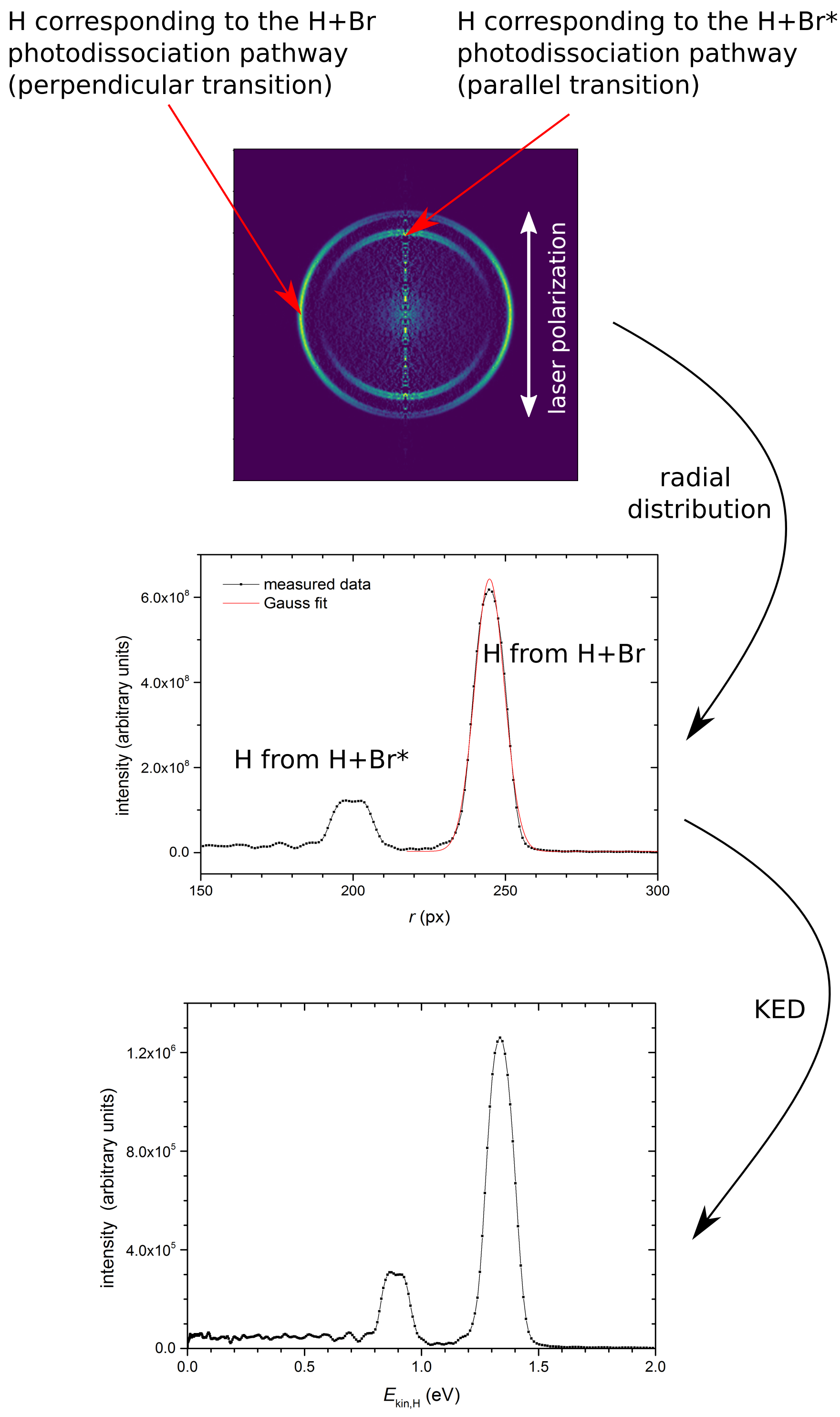

Figure 2.5: Calibration performed on HBr molecule: transformed image of H photofragments, corresponding radial distribution and KED (not normalized).

for the faster hydrogen (from the H+Br photodissociation channel). Based on the considerations in Chapter 1.2.1, we can easily determine the faster hydrogen's kinetic energy with the knowledge of the dissociation energy of HBr and fragments' masses as $E_{\mathrm{kin,H}} = 1.337\,\mathrm{eV}$. The calibration constant is then simply $K = E_{\mathrm{kin,H}}/r^2$, and can be used in further experiments to get KEDs from the radial distribution.

Calibration was performed on H^+ ions, but in this thesis we discuss the measurements of different ionic fragments. Therefore, the question arises whether the calibration is also applicable to the ions of other masses. Equation 2.31 gives the answer. We can see that measured energy is not a function of mass: $E_{\mathrm{kin}} \neq f(m)$. Calibration performed on H^+ can thus be used for ions of other masses as well.

2.4 Laser system

2.4.1 Description

For the photodissociation of molecules (or clusters) and for ionization of their fragments, two different lasers are usually needed. In our experiment, we use excimer and UV tunable laser, which are counterpropagating and spatially overlapping with the molecular beam inside the intersection region of the VMI chamber of AIM.

ArF excimer laser (Coherent ExciStar XS) with 5 ns pulse duration and 10 Hz repetition rate generates the radiation of wavelength $\lambda_{\mathrm{exc}} = 193.3\,\mathrm{nm}$, which is suitable for photodissociation. The laser beam is focused into the VMI vacuum chamber with a lens of focal length $f_0 = 50\,\mathrm{cm}$. To reach the required horizontal polarization, we use a thin film polarizer oriented at Brewster angle. The energy of the excimer laser pulse inside the intersection region is usually around 0.55 mJ.

The nanosecond tunable UV OPO laser (EKSPLA NT-230: the diode pumped Q-switched Nd:YAG laser and optical parametric oscillator, OPO) is used for REMPI and has a broad spectral range from 210 to 2600 nm. The laser generates pulses with 5 ns duration and is triggered at half the excimer laser repetition rate (5 Hz) so that we can measure the background signal. Synchronization of both lasers and pulsed nozzle generating the molecular beam pulse is driven by the delay generator (BNC 575). The UV OPO laser beam is focused into the VMI chamber intersection region with planoconvex and positive meniscus lenses with effective focal length $f_0 = 25\,\mathrm{cm}$. The energy of the UV OPO laser pulse inside the intersection region was usually around 0.60 mJ during our measurements with wavelengths $\lambda_{\mathrm{OPO}} \approx 235\,\mathrm{nm}$.

2.4.2 Laser spot size measurement and photon flux calculation

In order to achieve the best possible beam overlap in the AIM's intersection region, it is useful to know the approximate size of laser spot size in the focus.

For a beam width $w(z)$ of a general beam propagating along the z-axis applies equation

$$w(z) = w_0 \sqrt{1 + \left(\frac{M^2 \lambda}{\pi w_0^2} \right)^2 (z - z_0)^2}, \tag{2.32}$$

where M^2 represents the characteristic parameter of the beam, the measure of quality ($M^2 \geq 1$ with limit value $M^2 = 1$ for single-mode TEM_0 gaussian beam), λ is the wavelemght, w_0 is the beam width at the point of laser focus and z_0 is the location of the focus. [Siegman, 1998]

The spot diameters (i.e. $2w$) of both excimer and UV OPO (at wavelength $\lambda = 350\,\mathrm{nm}$) lasers were measured in x and y directions at several different positions along the beams propagation (z-axis) using the energy sensor and LabView program. The results fitted according to Equation 2.32 (multiplied by a factor of 2) are graphed in Figure 2.6 and 2.7. The location of the focus in x and y direction is different for both lasers. The fitted beam widths at the point of the laser focus w_0 are outlined in Table 2.1.

The laser focus diameters are schematically illustrated in Figure 2.8 (for simplicity it is neglected that the location of the focus z_0 is not the same in x and y direction).

Table 2.1: Beam widths at the point of laser focus w_0 in x and y direction for excimer and UV OPO laser.

	$w_{0,\,x}$ (μm)	$w_{0,\,y}$ (μm)
excimer (193 nm)	89.1(0.4)	149.1(0.8)
UV OPO (350 nm)	45.1(0.4)	62.7(0.7)

Now let us calculate the photon flux in the laser focus. Increased photon flux can cause multiphoton effects (e.g. two-photon ionization of the molecule followed by the photodissociaton of the ion, not the neutral molecule), as discussed in Vinklárek et al. [2020b]. The photon flux Φ is defined as the number of photons per unit area per second. During the measurements, laser energy per pulse E_{LP} was around $0.55\,\mathrm{mJ}$ and $0.60\,\mathrm{mJ}$ for excimer and UV OPO laser, respectively. Both lasers have a pulse duration $t_{\mathrm{LP}} = 5\,\mathrm{ns}$. The area of the laser focus can be estimated based on the laser spot size measurement above. The laser focus shape is approximated as a rectangle with area $A = 2w_{0,x} \cdot 2w_{0,y}$ (we are neglecting the focus shift in x and y). With the photon energy defined as $E_{\mathrm{photon}} = hc/\lambda$, where h is the Planck constant, c is the speed of light in vacuum and λ is the wavelength, the photon flux can be calculated as

$$\Phi = \frac{E_{\mathrm{LP}}}{t_{\mathrm{LP}} \cdot A \cdot E_{\mathrm{photon}}}. \tag{2.33}$$

The focus photon flux was calculated as $\Phi_{\mathrm{exc}} \sim 2 \cdot 10^{26}$ photons $\cdot\mathrm{cm}^{-2}\cdot\,\mathrm{s}^{-1}$ for excimer and $\Phi_{\mathrm{OPO}} \sim 2 \cdot 10^{27}$ photons $\cdot\mathrm{cm}^{-2}\cdot\,\mathrm{s}^{-1}$ for UV OPO laser.

The lasers enter the AIM interaction chamber through the wedged UV fused silica window. Here, approximately 10% of energy is lost due to reflection (for 193.1 and 350 nm wavelengths).

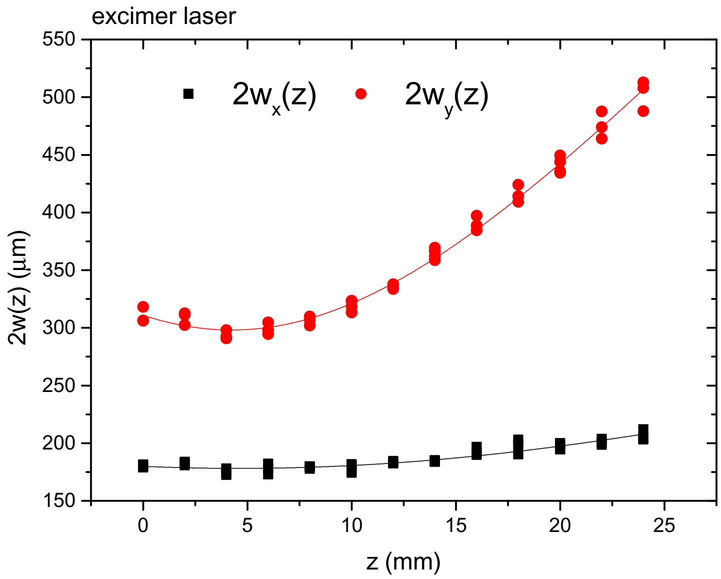

Figure 2.6: Beam diameter measurement for excimer laser.

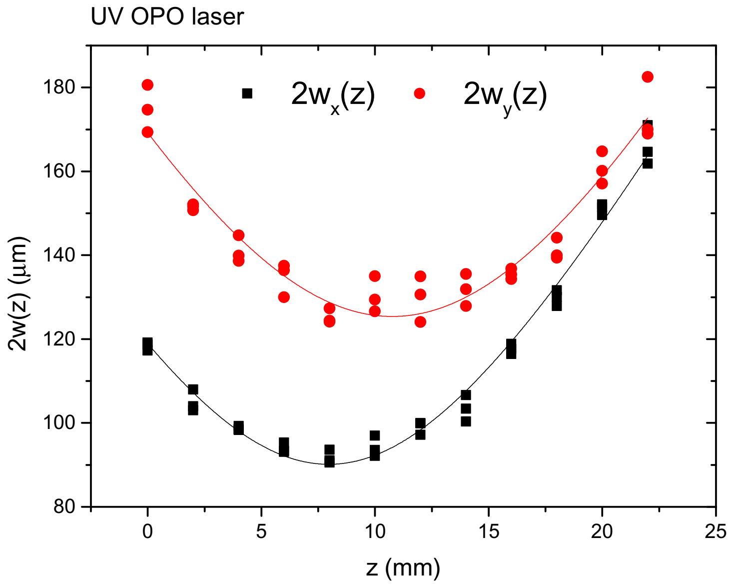

Figure 2.7: Beam diameter measurement for UV OPO laser.

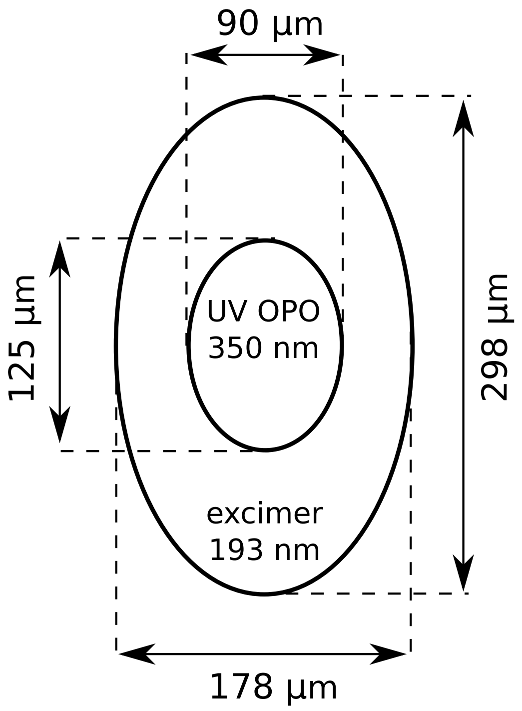

Figure 2.8: Focus size for excimer and UV OPO laser.

It ought be stressed that the above measurements and calculations are approximate, but sufficient for our needs.

3. Chloroalkanes

3.1 Motivation

In this thesis, the photodissociation dynamics along C–Cl reaction coordinate of three chloroalkanes (1-chloropropane, 2-chloropropane and 1-chloropentane) is studied and compared with previously measured photodissociation dynamics chloromethane [Vinklárek et al., 2020a]. The investigation of such systems is interesting from the atmospheric point of view as the stratospheric chlorine is identified to be one of the major threats for the ozone layer (see Chapter 1.1). In addition to chlorine, other halogens are also involved in the ozone-destroying catalytic cycles, bromine being especially effective [Solomon, 1999]. However, abundances of chlorine emitted by the human activity are much higher, so chlorine is still playing the leading role when it comes to the ozone destruction.

The global production of the ozone-depleting substances (ODSs) from human sources, for example CFCs, are controlled by the Montreal protocol. Halogen source gases of natural origin are not considered ODSs, and thus not regulated. [Fahey and Hegglin, 2011] The primary natural source gas of stratospheric chlorine is chloromethane CH_3Cl. Stratospheric chloromethane has both oceanic and terrestrial origin (notably biomass burning) [Fahey and Hegglin, 2011, Lobert et al., 1999], but there are still many questions regarding the formation of this gas and some large sources contributing to the global budget are unknown [Keppler et al., 2005, Bahlmann et al., 2019]. Also, although CH_3Cl is largely natural in origin, we still struggle with significant uncertainties regarding the rate of its emission from anthropogenic sources, despite a huge effort [Li et al., 2017]. In 2008, nearly 17% of the chlorine in the stratosphere was attributed to CH_3Cl [Fahey and Hegglin, 2011]. Therefore, it is essential to understand its both natural and anthropogenic sources for future global policies action, as chloromethane is expected to control the future abundances of stratospheric ozone, because the production of ODSs is gradually reduced [Bahlmann et al., 2019, Cristofanelli et al., 2020]. However, it ought to be noted that CH_3Cl of natural origin is not the cause of the massive ozone hole discovered in 1980s since natural chloromethane's abundances have not seem to increase since the second half of the last century [Fahey and Hegglin, 2011]. Whereas CH_3Cl is abundantly represented in the stratosphere, actual stratospheric abundances of the higher chloroalkanes studied in this thesis have not been reported to our best kowledge. Hodnebrog et al. [2020] include them in their review as less abundant compounds.

For all the reasons summarized above, the study of the photodissoiation and solvation properties of chloromethane is of high importance. The photodissociation of halogenoalkanes, especially halogenomethanes, have been largely examined over the last few decades, e.g. Riley and Wilson [1972], Kawasaki et al. [1984], Townsend et al. [2004], Corrales et al. [2014], Vinklárek et al. [2020a,b], Murillo-Sánchez et al. [2020]. Some of the studies have indicated that the changing alkyl chain length and varying halogen group position can have effect on the photofragments properties. In this thesis, we are investigating the changing photodissociation dynamics of the molecules with increasing structural complexity. We are comparing the dynamics of CH_3Cl with linearly prolonged n-C_3H_7Cl and

$n\text{-}C_5H_{11}Cl$ and branched $i\text{-}C_3H_7Cl$ (structures of all these molecules are illustrated in Figure 3.1). In all the cases we study the photodissociation of C–Cl bond for different R–Cl molecules, where R is the varying alkyl radical chain, using the VMI method. With $n\text{-}C_3H_7Cl$ and $n\text{-}C_5H_{11}Cl$ molecules, we are investigating the effect of the alkyl chain prolongation on photodissociation dynamics, with $n\text{-}C_3H_7Cl$ and $i\text{-}C_3H_7Cl$ the effect of the change of the chlorine group position. The changes in the alkyl chain and chlorine group position can have essential consequence for the molecule's energetics, alignment when attached a to cloud droplet (as has been indicated in theoretical simulations with chloromethane and 1-chloropentane adsorbed on the surface of watter clusters in Pasalic et al. [2011]), and thus reaction rates.

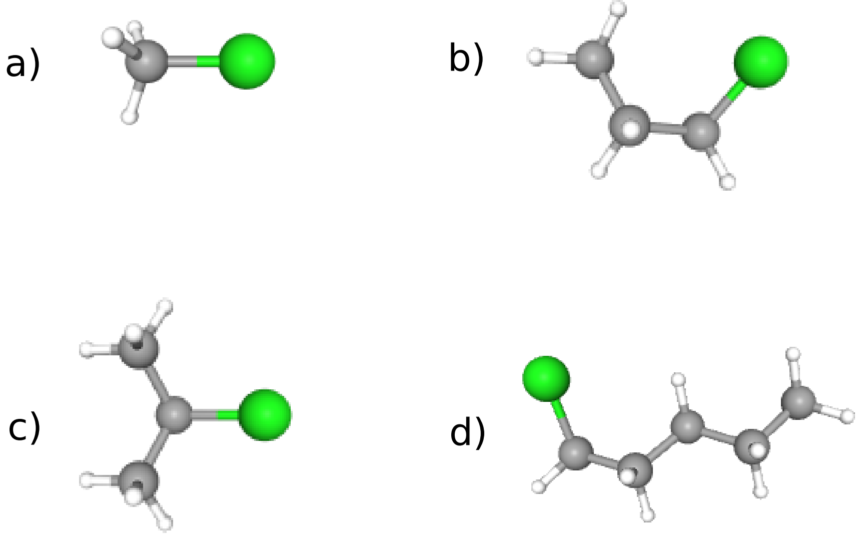

Figure 3.1: Structures of studied chloroalkanes: a) chloromethane (CH_3Cl), b) 1-chloropropane ($n\text{-}C_3H_7Cl$), c) 2-chloropropane ($i\text{-}C_3H_7Cl$), d) 1-chloropentane ($n\text{-}C_5H_{11}Cl$). Images taken from PubChem [2021].

3.2 Photodissociation of chloroalkanes

The Ã-band photodissociation of halogenomethanes follows two dominant fragmentation pathways. In the case of chloromethane, the Ã-band absorption continuum has the range from 165 to 230 nm, and the two dominant photofragmentation pathways are

$$\begin{aligned} \mathrm{CH_3Cl} + \hbar\omega \longrightarrow & \mathrm{CH_3} + \mathrm{Cl}(^2\mathrm{P}_{3/2}) \\ & \mathrm{CH_3} + \mathrm{Cl}^*(^2\mathrm{P}_{1/2}). \end{aligned}$$

Photon absorption leads to the electronic excitation of the molecule with three potential surfaces accessible, usually denoted $^3Q_1$, $^3Q_0$ and $^1Q_1$ in literature. Whereas the transitions to excited states $^1Q_1$ and $^3Q_1$ are of rather perpendicular nature (the value of anisotropy parameter β is close to 2) and lead to the ground-state chlorine fragment radical, $^3Q_0$ excited state is of rather parallel nature (β is close to -1) and leads to the spin-orbit excited Cl* fragment, as graphically shown in Figure 3.2. All the three states are repulsive and the process of dissociation is very quick, within $\sim$ fs. [Townsend et al., 2004]

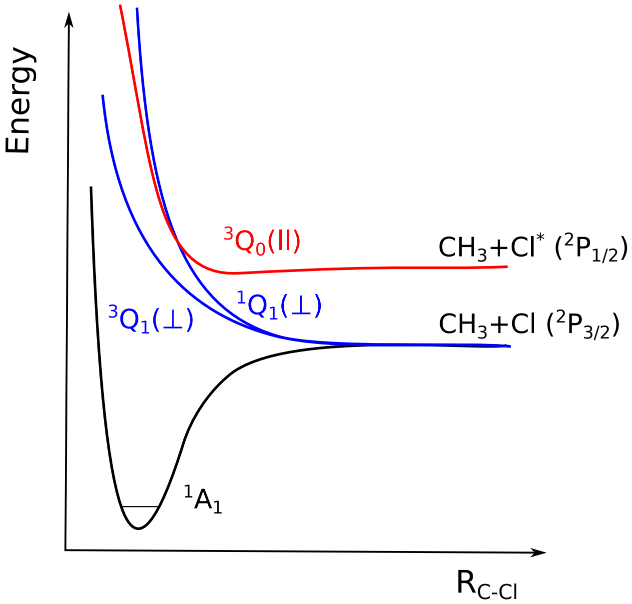

Figure 3.2: Schematic illustration of C–Cl photodissociation of CH_3Cl. Illustrarion according to Townsend et al. [2004].

During the interaction of the molecule with the photon, the symmetry of the system is lowered, which can result in strong coupling between $^1Q_1$ singlet and $^3Q_0$ triplet state. This enables intersystem crossing[1] as the molecule breaks apart (the conical intersection is occurring out of the Franck-Condon region) [Townsend et al., 2004]. The different photodissociation channels are reflected in the fragments' energies and angular distribution, which allows further reconstruction of the photodissociation dynamics of the molecule. Intersystem crossing is the strongest with the molecules containing heavy atoms – such as iodine or bromine. It will be later demonstrated in this thesis that in chlorinated molecules spin-orbit effect may also be well observed, especially for the molecules with long alkyl chain.

The transition to $^3Q_1$ surface is negligible compared with the transitions to $^3Q_0$ and $^1Q_1$. Also, there is a strong evidence that $^3Q_1$ does not participate in the intersystem crossing. Therefore, this potential surface will be further omitted from our considerations. [Townsend et al., 2004]

The C–Cl photodissociation PESs for higher chloroalkanes look similarly to CH_3Cl [Vinklárek et al., 2021].

---

[1] A process when a singlet state nonradiatively passes to a triplet state or vice versa.

4. Results

4.1 Experimental conditions and VMI images

The experiments were performed on AIM (described in Chapter 2.3). The VMI images of CH_3Cl were recorded previously by the group [Vinklárek et al., 2020a,b]. For this thesis, three higher chloroalkanes were measured, and the data obtained were then compared with the results from the CH_3Cl measurement. The expansion conditions are listed in Table 4.1. The He buffer gas passed through the reservoir, kept at the constant temperature T_r, containing the sample of the measured higher chloroalkane. The helium buffer gas was used to achieve non-clustering conditions. The seeded gas then supersonically expanded at the total stagnation pressure p_0 through the pulsed nozzle of diameter 0.6 mm and repetition rate 10 Hz. The molecules passed through the 1 mm skimmer, forming the beam of isolated molecules and entering the VMI detection chamber. Here, two counterpropagating and spatially overlapped laser beam pulses interacted with the molecular beam pulse. First, horizontally polarized radiation of the wavelength 193.3 nm generated by ArF excimer laser photodissociated the molecules, and second, radiation generated by UV OPO laser ionized the chlorine photofragments via (2+1) REMPI process. To prevent any mixed-multiphoton effect, the ionizing pulse arrived with 10–20 ns delay. Also, the ionizing UV OPO laser was running on the half repetition rate than excimer laser and pulsed nozzle (5 Hz) so that the background signal could be measured and later subtracted during the evaluation process. Both laser pulses and molecular beam pulse were synchronized by the delay generator. The chlorine fragments were ionized at wavelengths 235.305 nm for the ground-state Cl photofragment and 235.175 nm for the spin-orbit excited Cl* photofragment. The REMPI wavelengths were chosen according to Arepalli et al. [1985] and then adapted so that the best signal is reached. The REMPI schemes are:

$$\mathrm{Cl}\ 3\mathrm{p}(^2\mathrm{P}_{3/2}) \xrightarrow{2\hbar\omega} \mathrm{Cl}\ 4\mathrm{p}(^2\mathrm{P}_{1/2}) \xrightarrow{\hbar\omega} \mathrm{Cl}^+ \quad (235.305\ \mathrm{nm}),$$

$$\mathrm{Cl}^*\ 3\mathrm{p}(^2\mathrm{P}_{1/2}) \xrightarrow{2\hbar\omega} \mathrm{Cl}\ 4\mathrm{p}(^2\mathrm{D}_{3/2}) \xrightarrow{\hbar\omega} \mathrm{Cl}^+ \quad (235.175\ \mathrm{nm}).$$

The ionized chlorine photofragments were extracted by the VMI ion optics towards the detector. The extraction region is perpendicular to the plane defined by the laser beams and molecular beam, and ends with a gated MCP detector in chevron stack combined with a phosphor screen. After the ion detection, images were recorded by CCD camera. When the measured signal is not extremely strong, such as in our case with chloroalkanes, we apply centroiding algorithm to the measured data. A signal from a single ion usually covers relatively large number of pixels, and centroing algorithm determines the true position of the ion with a good accuracy. This, for example, may improve the resolution of the image, and the quality of the symmetry of the image. The raw collected images were transformed by the inverse Abel transformation so that the original 3D ion

Table 4.1: The higher chloroalkanes (Sigma-Aldrich) were seeded in He buffer gas. The expansion conditions are: T_r is the sample reservoir temperature, p_v and p_0 denote the vapour pressure of the sample and the total stagnation pressure of the expanding mixture, respectively. The vapour pressure was derived from the temperature through Antoine equation. For chloromethane (Sigma-Aldrich), a gas mixture of 7% CH_3Cl in He was used [Vinklárek et al., 2020a].

Molecule	CH_3Cl	n-C_3H_7Cl	i-C_3H_7Cl	n-$C_5H_{11}Cl$
T_r (°)	22.0	3.0	-24.5	20.0
p_v (bar)	0.12 (7%)	0.12	0.08	0.04
p_0 (bar)	1.7	1.8	1.8	1.8

velocity distribution is reconstructed. The more detailed description of the VMI method, AIM and the laser system can be found in Chapter 2.

The transformed images of Cl and Cl* photofragments of all the measured chloroalkanes are depicted in Figure 4.1. All the measured and transformed images exhibit a single ring corresponding to the photodissociation of the monomer, with the exception of i-C_3H_7Cl. Here, for both Cl and Cl* images we can see an additional signal of fragments with lower kinetic energy. That is visible in the images in Figure 4.1 or in KEDs that are presented later (Figure 4.3). The central signal may arise due to the clustering of chloroalkanes in the molecular beam or due to multiphoton processes. However, based on previous measurements [Vinklárek et al., 2020b], multiphoton processes can be excluded. On the other hand, clustering cannot be positively excluded. While for the other chloroalkanes conditions for monomer regime were always found, in the case of i-C_3H_7Cl we were not able to set the conditions so that there is no central intensity recorded. The VMI signal for i-C_3H_7Cl fragments was low, so further diluting of the expansion gas mixture was not possible. Not only clustering, but also residual background signal, which is always subtracted, may not be in this case eliminated completely because of the weak VMI signal. Still, the fast fragments' ring clearly corresponds to the Cl fragment velocity from the monomer dissociation, as it fits the other images recorded.

Directly from the raw images (that are not shown in this thesis), one can determine the branching ratios [Cl*]/[Cl] for the individual molecules. It can be done simply by summarizing the signal intensity data from the matrix of the raw image of Cl* and Cl fragment, and then dividing these two values[1]. The [Cl*]/[Cl] values calculated in this way must be, however, rescaled due to the different ionization efficiency of the ground-state and spin-orbit excited chlorine during REMPI process [Regan et al., 1999]. For CH_3Cl, the branching ratio should be [Cl*]/[Cl] = 0.86 according to Townsend et al. [2004]. All the other branching ratios has been rescaled by the calibration factor that has been used for CH_3Cl to reach the value of 0.86 in previous measurements [Vinklárek et al., 2020a]. Rescaled [Cl*]/[Cl] values are outlined in Table 4.2. It can be noticed that the uncertainties of the [Cl*]/[Cl] values are relatively large. That is mainly due

---

[1] Another approach is to integrate and divide the areas under the Cl* and Cl peak in the KED.

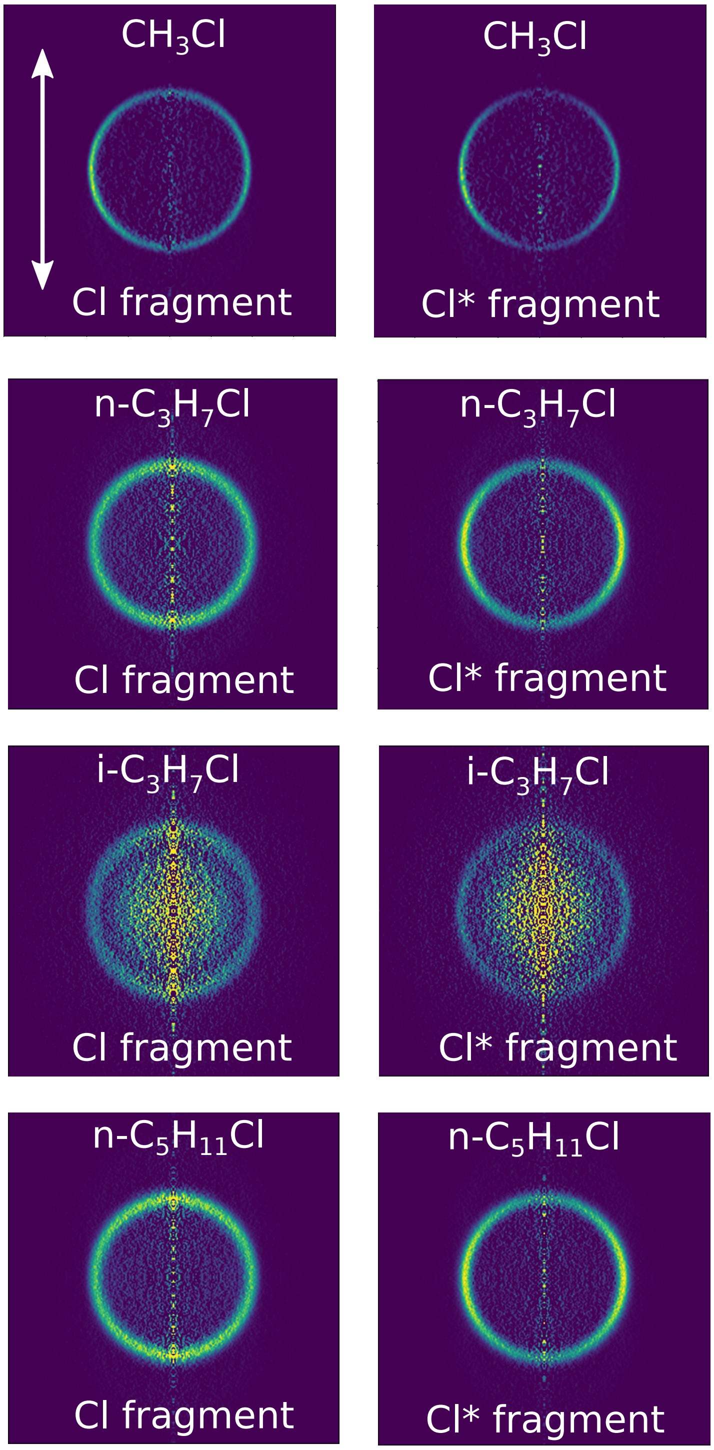

Figure 4.1: Transformed Cl and Cl* photofragment images of measured chloroalkanes. The arrow in the top image indicates the laser polarization.

to the fact that the VMI signal intensity fluctuates (usually decreases) in time, and it is not easy to keep it constant. VMI signal fluctuation is caused mainly by molecular beam intensity fluctuations and by decreasing lasers' intensities during the day. That is why we always try to measure both Cl and Cl* fragments of each molecule in one day, and carefully check the conditions. Even though, the estimated uncertainty is still large. The [Cl*]/[Cl] values will be needed later to determine the intersystem crossing probability.

Table 4.2: Rescaled branching ratio [Cl*]/[Cl] for measured chloroalkanes. Uncertainty of the value is in the parenthesis.

Molecule	CH_3Cl	n-C_3H_7Cl	i-C_3H_7Cl	n-$C_5H_{11}Cl$
[Cl*]/[Cl]	0.86	1.08(0.35)	0.53(0.35)	1.03(0.25)

4.2 TOF spectra

Even within the low-field mode suitable for VMI measurements, we can measure the TOF mass spectra on AIM as described in Chapter 2.3. The measurements were performed in continuous mode (no gating) in order to record all the masses, and with the UV OPO laser switched off. The background was also measured (meaning that the molecular beam was switched off) and subtracted. As an example, measured TOF mass spectrum of 1-chloropentane is shown in Figure 4.2 together with the mass spectrum from National Institute of Standards and Technology (NIST) [NIST, 2021] for comparsion. It ought to be mentioned that the NIST mass spectrum corresponds to the electron ionization (EI).

The resolution of TOF mass spectrum is low due to various reasons briefly discussed in Chapter 2.3. Yet we can see some resemblance to the spectrum from NIST, which means we generate only monomers and no clusters in our seeded expansion. Two sharp peaks in Figure 4.2 correspond to photons and hydrogen ions (peak is shifted due to calibration).

4.3 Available energy partitioning

First, let us have a look at the energy distribution of the system. As can be easily seen by comparing Figure 3.2 with Figure 1.1, chloroalkanes undergo direct photodissociation, which is described in Chapter 1.2.1. However, unlike the illustrative molecule AB, chloroalkanes have a manifold of electronic states and interstate dynamics. Let us go back to the Equation 1.1 describing the excess energy of the fragments after potodissociation (which is the total energy available) E_{ex}. From now on, this energy will be referred to as E_{tot} for better clarity, and modified so that it does not include the electronic degrees of freedom:

$$E_{tot} = \hbar\omega - D_0 + E^{\text{P}}_{\text{int}} - E_{\text{el}}, \tag{4.1}$$

where $\hbar\omega$ is the photon energy, D_0 is the dissociation energy required to break the C–Cl bond, $E^{\text{P}}_{\text{int}}$ is the parent molecule internal energy and E_{el} is the internal electronic energy of the fragment molecules. In all the measurements, the

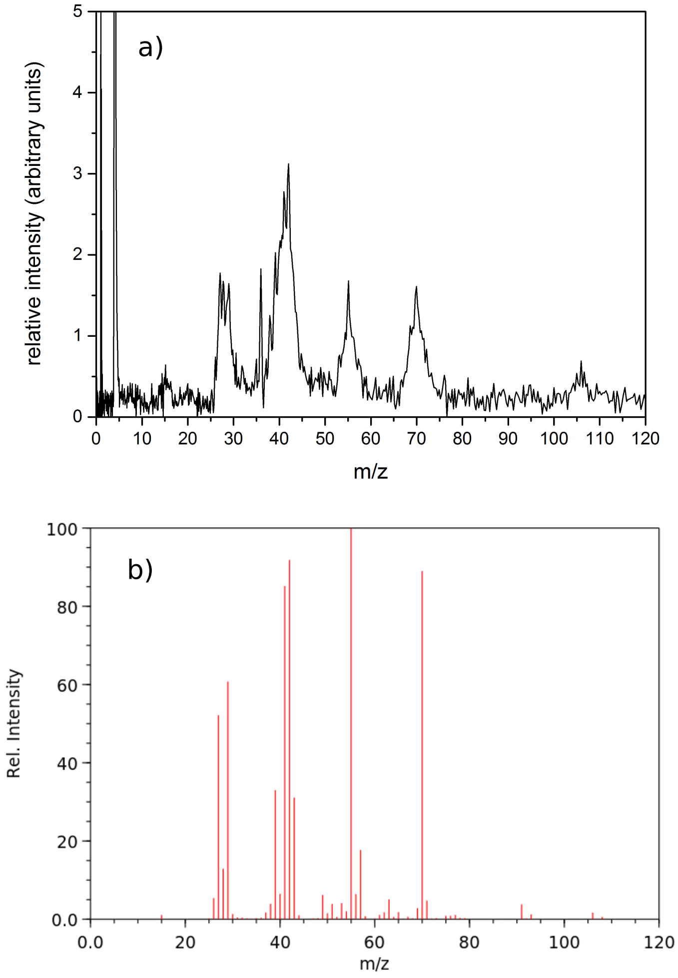

Figure 4.2: Mass spectrum of 1-chloropentane. a) Measured TOF spectrum on AIM. b) NIST mass spectrum (EI), taken from NIST [2021].

photon energy used for photodissociation was $\hbar\omega = 6.41$ eV. For the dissociation energies D_0, the experimentally determined values listed in the Table 4.3 were used in our calculations. Further, as our molecules generated in supersonic expansions are very cold, we assume that $E^{\mathrm{P}}_{\mathrm{int}} = 0$. The photodissociation of chloroalkanes follows two dominant pathways creating chlorine fragment in ground or excited electronic state. Ground state chlorine Cl has no internal electronic energy $E^{\mathrm{Cl}}_{\mathrm{el}} = 0$, for excited chlorine Cl*, the internal electronic energy corresponds to the energy level splitting caused by the spin–orbit interaction, $E^{\mathrm{Cl}^*}_{\mathrm{el}} = E_{\mathrm{SO}} = 0.109$ eV [Townsend et al., 2004]. In Table 4.4, the calculated values of total energy available E_{tot} are summarized for all the photodissociation pathways of the measured chloroalkanes. The total available energy values suggest that there is not enough energy for the C–C or C–H bonds to be broken. In other words, further fragmentation of alkyl fragment (which will be further denoted as R) is not energetically accessible, and thus we can assume the two-body dissociation.

Table 4.3: Experimental C–Cl bond dissociation energies D_0 of studied chloroalkanes in eV. The values are taken from Blanksby and Ellison [2003], Stevens et al. [2010] and Leal et al. [2001]. For n-C_3H_7Cl, no experimental value of D_0 has been reported to our knowledge, for this reason, we used the same value as for i-C_3H_7Cl.

Molecule	CH_3Cl	n-C_3H_7Cl	i-C_3H_7Cl	n-$C_5H_{11}Cl$
D_0 (eV)	3.565	3.635	3.635	3.653

Table 4.4: The calculated values of total energies available E_{tot} for the fragments after the photodissociation of chloroalkanes. Both dominant photodissociation pathways are considered, R denotes the alkyl fragment.

Molecule	CH_3Cl		n-C_3H_7Cl		i-C_3H_7Cl		n-$C_5H_{11}Cl$	
Pathway	R+Cl	R+Cl*	R+Cl	R+Cl*	R+Cl	R+Cl*	R+Cl	R+Cl*
E_{tot} (eV)	2.85	2.74	2.78	2.67	2.78	2.67	2.76	2.65

The total energy available E_{tot} is redistributed between the translational and internal energy of the photofragments, internal energy including rotational and vibrational degrees of freedom, $E_{\mathrm{tot}} = E_{\mathrm{tr}} + E_{\mathrm{int}} = E_{\mathrm{tr}} + E_{\mathrm{rot}} + E_{\mathrm{vib}}$.

4.3.1 Kinetic energy distribution measurement

The KEDs of Cl and Cl* photofragments were acquired from the transformed images (see Figure 4.1) by the standard integration method described in Chapter 2.2 for all the measured chloroalkanes, and are shown in Figure 4.3. All the narrow peaks, corresponding to the dissociation of monomers, were fitted by a Gaussian function to obtain the peak positions $E_{\mathrm{kin,\,Cl}}$, which represent the mean values of the chlorine fragment kinetic energies. The fitted peak positions $E_{\mathrm{kin,\,Cl}}$

and full width at half maximum (FWHM) of our Gaussian fits are listed in Table 4.5. Chlorine carries away similar kinetic energy (about 0.8 eV) regardless of the size of the alkyl. This suggests that chlorine is dissociating against carbon atom and not the whole alkyl. This assumption is used in the classical spectator model described later in this chapter.

Assuming the two-body photodissociation, we can use the law of conservation of energy and momentum and calculate the total translational energy E_{tr} of both fragments using the formula 1.4 derived already in Chapter 1.2.1

$$E_{\mathrm{tr}} = \frac{M}{m_{\mathrm{R}}} E_{\mathrm{kin,\,Cl}}, \tag{4.2}$$

where $E_{\mathrm{kin,\,Cl}}$ is the measured kinetic energy of chlorine fragment, M denotes the mass of the whole molecule before photodissociation and m_{R} is the mass of the alkyl fragment. Now, as we know both total and translational energy, we can determine the extent of internal excitation as

$$f_{\mathrm{int}} = \frac{E_{\mathrm{int}}}{E_{\mathrm{tot}}} = 1 - \frac{E_{\mathrm{tr}}}{E_{\mathrm{tot}}}. \tag{4.3}$$

The internal energy corresponds to vibrations and rotations, and thus goes all into alkyl fragment excitation, as chlorine fragment can be excited only electronically. The calculated values of E_{tr} and f_{int} are outlined in Table 4.5. From the values of f_{int} we see that while in the case of CH_3Cl less than 10% of the available energy goes into the alkyl radical internal energy, in all the other higher chloroalkanes it is about 40–60%.

Table 4.5: The fitted maximum peak positions $E_{\mathrm{kin,\,Cl}}$ (reflecting the mean kinetic energy of the chlorine fragments) and corresponding FWHM. The calculated values of the total translational energy E_{tr} and the extent of the internal excitation of the alkyl fragment f_{int}.

Molecule	CH_3Cl		n-C_3H_7Cl		i-C_3H_7Cl		n-$C_5H_{11}Cl$	
Fragment	Cl	Cl*	Cl	Cl*	Cl	Cl*	Cl	Cl*
$E_{\mathrm{kin,\,Cl}}$ (eV)	0.80	0.78	0.82	0.83	0.87	0.91	0.81	0.83
FWHM (eV)	0.13	0.11	0.27	0.21	0.35	0.27	0.27	0.22
E_{tr} (eV)	2.69	2.62	1.49	1.51	1.59	1.66	1.21	1.24
f_{int}	0.06	0.04	0.46	0.43	0.43	0.38	0.56	0.53

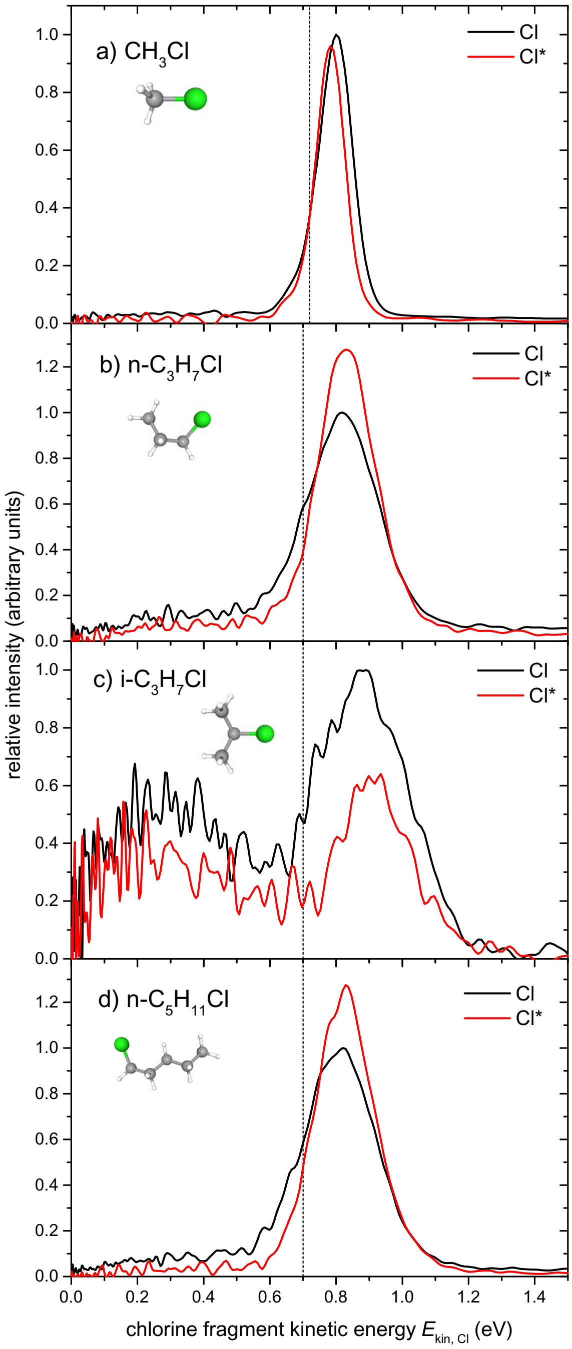

Figure 4.3: The KEDs of chlorine fragments of studied chloroalkanes. The dashed lines indicate the calculated ground-state chlorine kinetic energies within the spectator model classic approach. The spectra intensities are normalized so that the population ratios [Cl*]/[Cl] are preserved, and scaled to the maximum intensity of ground-state Cl for each molecule. The images of the structures of chloroalkanes are taken from PubChem [2021].

4.3.2 Classical mechanics models for energy distribution

We can compare measured results discussed above with calculations based on simple impulsive models that were proposed in 70's [Riley and Wilson, 1972, Busch and Wilson, 1972, Holdy et al., 1970]. First, let us assume that all the available energy E_{tot} goes into the translation of the fragments. This approach can be called a **hard spheres model** as the two fragments are considered to gain no internal energy E_{int}. From the law of conservation of energy and momentum, we can easily derive formula for kinetic energy of chlorine fragment

$$E^{\mathrm{HS}}_{\mathrm{kin,\,Cl}} = \frac{m_{\mathrm{R}}}{M} E_{\mathrm{tot}}. \tag{4.4}$$

The kinetic energy calculated in this way is the upper limit for the kinetic energy which can be reached by the fragment. Calculated values of $E_{\mathrm{kin,\,Cl}}$ are outlined in Table 4.6. For higher chloroalkanes, all the calculated values are overestimation of the values measured, which was expected. For CH_3Cl, the model values are in good agreement with the experiment. That is because less than 10% of available energy goes into CH_3 fragment, as has been demonstrated above, making the fragment a fairly good approximation of a hard sphere.

Spectator model for energy partitioning was introduced in Holdy et al. [1970] for photodynamics of triatomic molecules and later applied to photodynamics of iodoalkanes in Riley and Wilson [1972]. This model considers the photon absorption of the molecule to be quasidiatomic – this means that it assumes all the internal excitation of the fragments coming from the change in the potential energy along the breaking bond, and it omits other sources of internal excitation, for example the changes in the equilibrium bond angles [Holdy et al., 1970]. Thus, in our case of chloroalkanes, all the available energy E_{tot} and momentum is initially stored in the translation of the two atoms C and Cl between which the bond is broken. Atom C then interacts with the rest of the alkyl, which until then acted as a spectator. Momentum stays the same but part of the carbon's kinetic energy is redistributed between rotation and vibration of the alkyl fragment. Total available and total translational energy of the fragments can be expressed as

$$E_{\mathrm{tot}} = E_{\mathrm{kin,\,C}} + E_{\mathrm{kin,\,Cl}} = \frac{1}{2}\left(\frac{p_{\mathrm{C}}^2}{m_{\mathrm{C}}} + \frac{p_{\mathrm{Cl}}^2}{m_{\mathrm{Cl}}}\right), \tag{4.5a}$$

$$E_{\mathrm{tr}} = E_{\mathrm{kin,\,R}} + E_{\mathrm{kin,\,Cl}} = \frac{1}{2}\left(\frac{p_{\mathrm{R}}^2}{m_{\mathrm{R}}} + \frac{p_{\mathrm{Cl}}^2}{m_{\mathrm{Cl}}}\right). \tag{4.5b}$$

Using the momentum conservation $p_{\mathrm{Cl}} = p_{\mathrm{C}} = p_{\mathrm{R}}$ we can write

$$\frac{E_{\mathrm{tr}}}{E_{\mathrm{tot}}} = \frac{\frac{1}{m_{\mathrm{R}}} + \frac{1}{m_{\mathrm{Cl}}}}{\frac{1}{m_{\mathrm{C}}} + \frac{1}{m_{\mathrm{Cl}}}} = \frac{\mu_{\mathrm{a}}}{\mu_{\mathrm{f}}}, \tag{4.6}$$

where μ_{a} denotes the reduced mass[1] of C and Cl atoms and μ_{f} the reduced mass of R and Cl fragments. Energy corresponding to the chlorine fragment kinetic energy in the spectator model approach can be calculated as

$$E^{\mathrm{SP}}_{\mathrm{kin,\,Cl}} = \frac{\frac{1}{m_{\mathrm{Cl}}}}{\frac{1}{m_{\mathrm{C}}} + \frac{1}{m_{\mathrm{Cl}}}} E_{\mathrm{tot}} = \frac{m_{\mathrm{C}}}{m_{\mathrm{C}} + m_{\mathrm{Cl}}} E_{\mathrm{tot}}. \tag{4.7}$$

---

[1] $\frac{1}{\mu} = \frac{1}{m_1} + \frac{1}{m_2}$

The calculated values of $E^{\mathrm{SP}}_{\mathrm{kin,\,Cl}}$ for studied chloroalkanes are outlined in Table 4.6 and marked in Figure 4.3. The extent of internal excitation, that goes into R-fragment, can be simply determined by the energy conservation as

$$f^{\mathrm{SP}}_{\mathrm{int}} = \frac{E_{\mathrm{int}}}{E_{\mathrm{tot}}} = 1 - \frac{\mu_{\mathrm{a}}}{\mu_{\mathrm{f}}}. \tag{4.8}$$

Again, these values can be found in Table 4.6. It should be noted that the calculation of $f^{\mathrm{SP}}_{\mathrm{int}}$ within the spectator model cannot distinguish between the two dominant chloroalkane photodissociation pathways. While the hard spheres model model gives us the upper limit, spectator model underestimates the measured results. Also, we have to keep in mind that the classic calculations operate with the maximum kinetic energies possible within the model given, and our experimental kinetic energies correspond to mean values based on the Gaussian fit of the measured peaks.

Table 4.6: Kinetic energies of Cl and Cl* chlorine photofragment calculated from the hard spheres model ($E^{\mathrm{HS}}_{\mathrm{kin,\,Cl}}$) and spectator model ($E^{\mathrm{SP}}_{\mathrm{kin,\,Cl}}$). The extent of energy (independent of photodissociation pathway) which goes into alkyl fragment internal excitation in the approach of spectator model ($f^{\mathrm{SP}}_{\mathrm{int}}$) and rigid spectator model ($f^{\mathrm{RS}}_{\mathrm{int}}$). Experimental values $E_{\mathrm{kin,\,Cl}}$ and f_{int} are listed here again for comparison.

Molecule	CH_3Cl		n-C_3H_7Cl		i-C_3H_7Cl		n-$C_5H_{11}Cl$	
Fragment	Cl	Cl*	Cl	Cl*	Cl	Cl*	Cl	Cl*
$E_{\mathrm{kin,\,Cl}}$ (eV)	0.80	0.78	0.82	0.83	0.87	0.91	0.81	0.83
$E^{\mathrm{HS}}_{\mathrm{kin,\,Cl}}$ (eV)	0.85	0.81	1.52	1.46	1.52	1.46	1.84	1.77
$E^{\mathrm{SP}}_{\mathrm{kin,\,Cl}}$ (eV)	0.72	0.69	0.70	0.67	0.70	0.67	0.70	0.67
f_{int}	0.06	0.04	0.46	0.43	0.43	0.38	0.56	0.53
$f^{\mathrm{SP}}_{\mathrm{int}}$	0.15		0.54		0.54		0.62	
$f^{\mathrm{RS}}_{\mathrm{int}}$	0.00		0.22		0.22		0.21	

In the spectator model we assumed that the α-carbon[1] is weakly bound to the rest of the alkyl fragment, transferring part of its kinetic energy into both rotation and vibration. Riley and Wilson [1972] presents yet another limit of the quasi-diatomic model assuming that the alkyl bonds are infinitely stiff. We will call this approach a **rigid spectator model** as the recoiling alkyl fragment is a rigid body. Under this assumption, only the rotational excitation is allowed. The extent of this excitation can be expressed from the law of conservation of energy and linear and angular momentum as

$$f^{\mathrm{RS}}_{\mathrm{int}} = \frac{E_{\mathrm{int}}}{E_{\mathrm{tot}}} = \frac{E_{\mathrm{rot}}}{E_{\mathrm{tot}}} = \left(1 + \frac{I}{\mu_{\mathrm{f}} r_{\mathrm{cm}}^2 \sin^2\chi}\right)^{-1}, \tag{4.9}$$

where r_{cm} is the distance between α-carbon and the centre-of-mass of the alkyl fragment, I is the moment of inertia of the alkyl fragment around the axis through

---

[1] The α-carbon is the first carbon attached to chlorine in the chloroalkane.

its centre-of-mass which is perpendicular to the plane defined by the centre-of-mass, α-carbon and chlorine atom and χ is the angle between C–Cl bond and line between α-carbon and center-of-mass of the alkyl. If we consider the alkyl fragment to be a set of mass points, the position of the centre-of-mass can be determined as $\mathbf{x_T} = \sum_{i=1}^{n} m_i \mathbf{x_i} / m_\mathrm{R}$, where m_i are the masses of individual atoms, $\mathbf{x_i}$ their Cartesian coordinates and m_R is the mass of the whole alkyl. Again, it should be noted, that the values $f_\mathrm{int}^\mathrm{RS}$ do not take into consideration the two pathways possible for the photodissociation of chloroalkanes.

The moment of inertia of the alkyl can be determined as $I = \sum_{i=1}^{n} m_i r_i^2$, where m_i are again the masses of individual atoms and r_i their perpendicular distances from the axis of rotation. With the knowledge of the Cartesian coordinates of the individual atoms of the chloroalkane molecules, it is possible to determine the perpendicular distances r_i on the basis of geometric calculations.[1] These coordinates were provided by Petr Slavíček and Jiří Suchan from the Theoretical Photochemistry Research Group of University of Chemistry and Technology in Prague (see Attachement A.1). Calculated values of $f_\mathrm{int}^\mathrm{RS}$ are outlined in Table 4.6. We can see that for CH_3Cl, no energy goes into the internal excitation of the alkyl photofragment CH_3 in the rigid spectator approach. That is due to the fact that the alkyl's centre-of-mass lies in one axis with the C and Cl atoms (we assume that the fragments dissociate along the bond, thus, based on classical and geometric considerations, no energy can go into rotation). The results are also graphed in Figure 4.4, together with the results based on our measurement and spectator model. It is visible that the values for the extent of internal excitation based on experiment and spectator model follow the same pattern. Also, we can see that the values based on the experiment lie between the spectator and rigid spectator values. Similar result was obtained by Riley and Wilson [1972] for iodoalkanes. It seems that from the classic point of view, the photodissociation of halogenalkanes involves a recoil of semi-rigid alkyl fragment.

Now, let us go back to the spectator model and discuss the channeling of the internal excitation between the rotation and vibration. Holdy et al. [1970] and Busch and Wilson [1972] consider a triatomic molecule which dissociates with a bond angle α, and its recoiling diatomic fragment remains a rigid dumbbell. The momentum component perpendicular to the bond of the dumbbell contributes to the rotation and the parallel component contributes to the vibration (the dumbbell can be approximated as a harmonic oscillator). Within the spectator model, a simple derivation yields

$$f_\mathrm{rot}^\mathrm{SP} = \frac{E_\mathrm{rot}}{E_\mathrm{tot}} = f_\mathrm{int}^\mathrm{SP} \sin^2 \alpha, \tag{4.10a}$$

$$f_\mathrm{vib}^\mathrm{SP} = \frac{E_\mathrm{vib}}{E_\mathrm{tot}} = f_\mathrm{int}^\mathrm{SP} \cos^2 \alpha. \tag{4.10b}$$

We can extend this model to our polyatomic chloroalkanes with α being the angle between the breaking bond and line between the α-carbon and the centre-of-mass of the alkyl. Calculated values are outlined in Table 4.7. However, it has to be mentioned that this approach is a huge simplification, because alkyl fragment is

---

[1] We can assume that the geometry of initial excited and ground state is similar (Franck-Condon principle), and therefore we can use the Cartesian coordinates of the ground-state molecule for our calculation of $f_\mathrm{int}^\mathrm{RS}$ [Riley and Wilson, 1972].

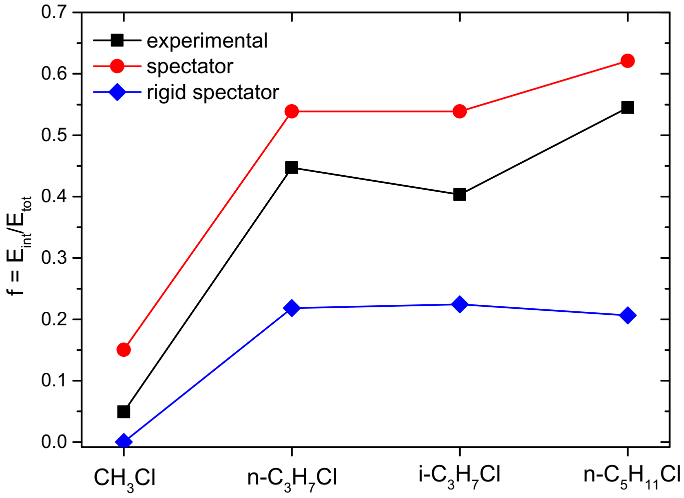

Figure 4.4: The fraction of the total energy available E_{tot} which goes into internal energy of the alkyl fragment plotted against the parent molecule identity (arbitrary scale). Black colour represents the values based on our experiment, red and blue represents the values based on the spectator and rigid spectator approach, respectively. The values of $E_{\mathrm{int}}/E_{\mathrm{tot}}$ are independent of the photodissociation pathway for the spectator and rigid spectator model. For the experimental points, the averaged values for R+Cl and R+Cl* fragmentation are plotted.

a radical with complex geometry and with many different modes of vibration, it is surely not a dumbbell-like harmonic oscillator. We cannot compare the calculated values with the measurement due to the fact that our nanosecond experiment cannot distinguish the internal energy partitioning. Nevertheless, we can compare the calculations with the measurements of Corrales et al. [2014], who investigated the dynamics of different linear and branched iodoalkanes using the femtosecond time-resolved VMI spectroscopy. Their results indicate different dynamics behaviour for linear and branched molecules. For linear molecules, internal energy of R radical fragment increases with increasing chain length and the dissociation process is dominated by a large amplitude rotational motion of the R-fragment. For branched molecules, the situation is different, the amount of energy that goes into the internal exitation decreases or stabilizes (in the case of i-C_3H_7I, which is indicated to represent an intermediate case between a pure linear and a pure branched molecule) comparing to their linear counterparts. Energy flux into branched iodoalkanes seems to be less effective. These results were supported by full-dimension time-resolved dynamics calculations. We could expect analogous dynamic behaviour for our studied chloroalkanes. Extent of rotational and vibrational energy that goes into R alkyl as outlined in Table 4.7, however, does not support such results – probably because of oversimplification of the model of the partitioning. Nevertheless, measured and calculated data depicted in Figure 4.4 qualitatively agree with the conclusions of Corrales et al. [2014].

Table 4.7: The fraction of the total energy available which goes into internal energy $f_{\mathrm{int}}^{\mathrm{SP}}$ within the spectator model, and partitioning between rotation $f_{\mathrm{rot}}^{\mathrm{SP}}$ and vibration $f_{\mathrm{vib}}^{\mathrm{SP}}$.

Molecule	CH_3Cl	n-C_3H_7Cl	i-C_3H_7Cl	n-$C_5H_{11}Cl$
$f_{\mathrm{int}}^{\mathrm{SP}}$	0.15	0.54	0.54	0.62
$f_{\mathrm{rot}}^{\mathrm{SP}}$	0.00	0.27	0.33	0.26
$f_{\mathrm{vib}}^{\mathrm{SP}}$	0.15	0.27	0.21	0.36

The partitioning of the internal energy between vibrational and rotational degrees of freedom of the R fragment is subtle, and unfortunately we cannot access it experimentally in our laboratory.

4.4 Angular distribution and intersystem crossing

Above, we analysed the energy partitioning of the studied chloroalkanes after photodissociation based on our measurements and classical impulsive models. However, photodissociation is a vector process and additional important information regarding the dynamics is hidden in the angular distribution, which can be obtained from the measured images using the standard integration method described in Chapter 2.2. The left sides of the images (see Figure 4.1) were integrated over the monomer region from 10° to 170° (measured from the bottom of the image) to avoid the noise in the middle of the images, which is caused by the Abel transformation. Figure 4.5 shows the resulting distribution for all chloroalkanes measured. For both Cl and Cl* photofragments, the fitted anisotropy parameters β are outlined in Table 4.8. The uncertainties of fits are underestimated compared to the actual measurement uncertainty. Therefore, the outlined uncertainties are estimated. The branching ratios [Cl*]/[Cl], discussed previously, are also listed in the same Table 4.8.

Table 4.8: The fitted anisotropy parameters β and the branching ratio [Cl*]/[Cl] for measured chloroalkanes. Uncertainty of the value is in the parenthesis.

Molecule	CH_3Cl	n-C_3H_7Cl	i-C_3H_7Cl	n-$C_5H_{11}Cl$
β (Cl)	-0.39(0.07)	0.12(0.08)	0.29(0.12)	0.18(0.08)
β (Cl*)	-0.67(0.08)	-0.38(0.08)	-0.14(0.12)	-0.30(0.08)
[Cl*]/[Cl]	0.86	1.08(0.35)	0.53(0.35)	1.03(0.25)

Let us go back to the Figure 3.2 for a while. The PES for CH_3Cl and higher chloroalkanes (as their dissociation curves are similar) indicate that there are two dominant dissociation pathways. Transition to the $^1Q_1$ state from the ground state $^1A_1$ is perpendicular (extreme value $\beta = 2$) and correlates with the formation of ground-state Cl, whereas transition to the $^3Q_0$ state is parallel (extreme value $\beta = -1$) and correlates with the formation of spin-orbit excited Cl*. In

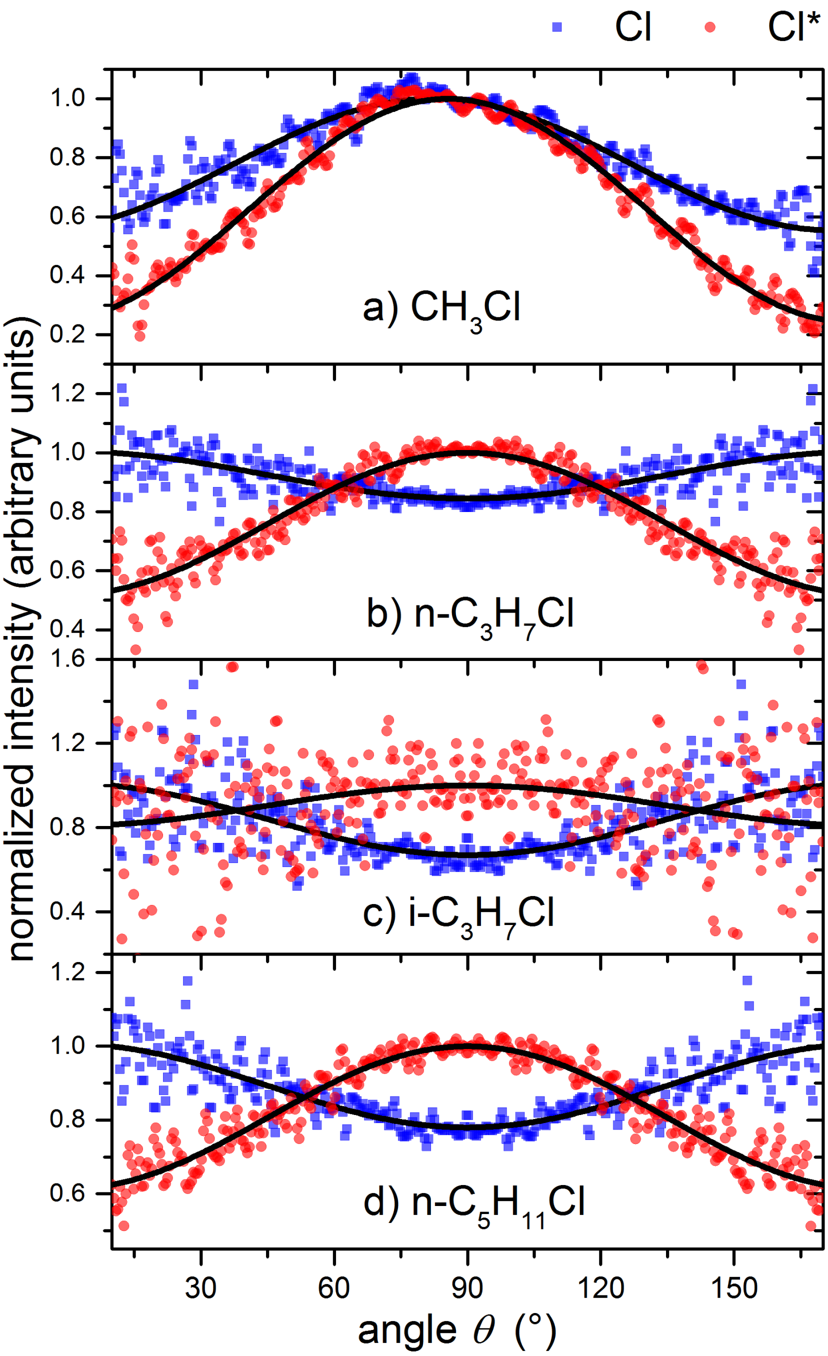

Figure 4.5: The angular distribution of measured chloroalkanes for both Cl and Cl* fragments. Corresponding images can be seen in Figure 4.1. The data are fitted according to the formula $I(\theta) \approx 1 + \beta P_2(\cos\alpha)$ (see Chapter 1.4).

contrast to Figure 3.2, the character of fitted anisotropy parameters β in Table 4.8 is slightly parallel or isotropic (β close to 0) for the ground-state Cl fragments of higher chloroalkanes (CH_3Cl is an exception having rather perpendicular character of β) and rather perpendicular for the spin-orbit excited Cl* fragments of all measured chloroalkanes. This discrepancy is caused by the intersystem crossing between the two states $^1Q_1$ and $^3Q_0$, and interaction which allows the transition between the states of different character. Townsend et al. [2004] suggest a simple model to determine the probability of the intersystem crossing in CH_3Cl photodissociation described below.

The photofragment anisotropy parameter that we gained from the measurement can be expressed as the weighted sum of the β-parameters corresponding to transitions to the excited states accessible:

$$\beta = \sum_i a_i \beta_i, \tag{4.11}$$

where the coeficients a_i are normalized,

$$\sum_i a_i = 1. \tag{4.12}$$

In our case, the transition to the two states $^1Q_1$ and $^3Q_0$ are dominant, therefore,

$$\beta_{\mathrm{exp}}(\mathrm{Cl}) = a_1 \beta_{^3\mathrm{Q}_0} + a_2 \beta_{^1\mathrm{Q}_1}, \tag{4.13a}$$

$$\beta_{\mathrm{exp}}(\mathrm{Cl}^*) = b_1 \beta_{^3\mathrm{Q}_0} + b_2 \beta_{^1\mathrm{Q}_1}. \tag{4.13b}$$

For $^1Q_1$ and $^3Q_0$ transitions, Townsend et al. [2004] expect the extreme theoretical values of $\beta_{^1\mathrm{Q}_1} = -1.0$ and $\beta_{^3\mathrm{Q}_0} = +2.0$, due to the fact that the dissociation is considerably faster than the molecular rotation period. However, these values are shifted in reality due to nonlinear geometry of the chloroalkane molecule during the absorption of the photon. The alkyl chain orientation has a strong influence on the orientation of the transition dipole moment, which is no longer dictated solely by the C–Cl bond orientation. This results in more isotropic absorption symmetry. The corrected anisotropy parameters β_{corr} were fitted from the simulated angular profiles of absorption transition by Petr Slavíček and Jiří Suchan [Vinklárek et al., 2021] and are shown in Table 4.9.

Table 4.9: Corrected anisotropy parameters for transitions $^1A_1 \to ^1 Q_1$ and $^1A_1 \to ^3 Q_0$.

Molecule	CH_3Cl	n-C_3H_7Cl	i-C_3H_7Cl	n-$C_5H_{11}Cl$
$\beta_{\mathrm{corr}}(^1\mathrm{Q}_1)$	-0.78	-0.40	-0.41	-0.32
$\beta_{\mathrm{corr}}(^3\mathrm{Q}_0)$	1.98	1.84	1.87	1.71

Even from the expansion coefficients a_i and b_i, outlined in Table 4.10, we can say something about the dissociation of the studied systems. In particular, we can determine how much chlorine fragments (Cl or Cl*) comes from diabatic (no mixing of states) and how much from adiabatic (intersystem crossing) dissociation.

Coefficient a_1 and a_2 correspond to the adiabatic and diabatic generation of the ground-state chlorine Cl, respectively. It can be seen that for higher chloroalkanes the significance of the adiabatic generation of Cl is increasing. One could therefore expect that the probability of the direct absorption into the state $^3\mathrm{Q}_0$ is increasing with the alkyl fragment. This hypothesis will be confirmed on the basis of further calculations.

Table 4.10: The expansion coefficients a_i and b_i calculated with the corrected β-parameters β_{corr}.

Molecule	CH_3Cl	n-C_3H_7Cl	i-C_3H_7Cl	n-$C_5H_{11}Cl$
a_1	0.14	0.23	0.31	0.25
a_2	0.86	0.77	0.69	0.75
b_1	0.04	0.01	0.12	0.01
b_2	0.96	0.99	0.88	0.99

Let us now return to the derivation of the intersystem crossing probability. From the branching ratio [Cl*]/[Cl] we can calculate the photofragment quantum yield as

$$\Phi_{\mathrm{Cl}} = \frac{[\mathrm{Cl}]}{[\mathrm{Cl}] + [\mathrm{Cl}^*]} = \frac{1}{1 + \frac{[\mathrm{Cl}^*]}{[\mathrm{Cl}]}}, \tag{4.14a}$$

$$\Phi_{\mathrm{Cl}^*} = 1 - \Phi_{\mathrm{Cl}}. \tag{4.14b}$$

Knowing the quantum yield, we can express the fractions that are contributing to the final products for each of the pathways:

$$f_{^3\mathrm{Q}_0\to{}^1\mathrm{Q}_1} = a_1\Phi_{\mathrm{Cl}}, \tag{4.15a}$$

$$f_{^1\mathrm{Q}_1} = a_2\Phi_{\mathrm{Cl}}, \tag{4.15b}$$

$$f_{^3\mathrm{Q}_0} = b_1\Phi_{\mathrm{Cl}^*}, \tag{4.15c}$$

$$f_{^1\mathrm{Q}_1\to{}^3\mathrm{Q}_0} = b_2\Phi_{\mathrm{Cl}^*}. \tag{4.15d}$$

From that we are finally able to evaluate the probability of the intersystem crossing and the probabilities of the direct absorption to $^1\mathrm{Q}_1$ and $^3\mathrm{Q}_0$ states,

$$P_{^1\mathrm{A}_1\to{}^1\mathrm{Q}_1} = f_{^1\mathrm{Q}_1} + f_{^1\mathrm{Q}_1\to{}^3\mathrm{Q}_0}, \tag{4.16a}$$

$$P_{^1\mathrm{A}_1\to{}^3\mathrm{Q}_0} = f_{^3\mathrm{Q}_0} + f_{^3\mathrm{Q}_0\to{}^1\mathrm{Q}_1}, \tag{4.16b}$$

$$P_{^3\mathrm{Q}_0\to{}^1\mathrm{Q}_1} = \frac{f_{^3\mathrm{Q}_0\to{}^1\mathrm{Q}_1}}{f_{^3\mathrm{Q}_0} + f_{^3\mathrm{Q}_0\to{}^1\mathrm{Q}_1}}, \tag{4.16c}$$

$$P_{^1\mathrm{Q}_1\to{}^3\mathrm{Q}_0} = \frac{f_{^1\mathrm{Q}_1\to{}^3\mathrm{Q}_0}}{f_{^1\mathrm{Q}_1} + f_{^1\mathrm{Q}_1\to{}^3\mathrm{Q}_0}}. \tag{4.16d}$$

The calculated probabilities are listed in Table 4.11. We can say that most of the Cl and Cl* fragments come from the direct absorption to the singlet state $^1\mathrm{Q}_1$. The direct absorption to the triplet state $^3\mathrm{Q}_0$ is becoming slightly more important for the higher chloroalkanes, however, its probability is still lower than the probability of absorption to the singlet state. The position of chlorine group turned out to have considerable impact on the probability of direct transition into the triplet state. In the case of i-C_3H_7Cl, the probability of direct transition into the triplet state is doubled compared with n-C_3H_7Cl. The geometry of i-C_3H_7Cl is enhancing the triplet state absorption rates, but reducing the probability of the intersystem crossing. The alkyl extension from n-C_3H_7Cl to n-$C_5H_{11}Cl$ does not show any significant differences in the calculated probabilities. The added carbons are apparently too distant from the C–Cl bond to have a visible effect.

Table 4.11: The probabilities of absorption to $^1Q_1$ and $^3Q_0$ states and probabilities of intersystem crossing $^3Q_0 \rightarrow ^1 Q_1$ and $^1Q_1 \rightarrow ^3 Q_0$. The values are calculated considering the corrected β-parameters β_{corr}.

Molecule	CH_3Cl	n-C_3H_7Cl	i-C_3H_7Cl	n-$C_5H_{11}Cl$
$P_{^1A_1 \rightarrow ^1Q_1}$	0.91	0.88	0.76	0.87
$P_{^1A_1 \rightarrow ^3Q_0}$	0.09	0.12	0.24	0.13
$P_{^1Q_1 \rightarrow ^3Q_0}$	0.49	0.58	0.41	0.58
$P_{^3Q_0 \rightarrow ^1Q_1}$	0.80	0.96	0.82	0.96

For comparison, we have also calculated the probabilities of direct absorptions and intersystem crossing assuming the extreme values $\beta_{^1Q_1} = -1.0$ and $\beta_{^3Q_0} = +2.0$, see Table 4.12. The probabilities for CH_3Cl are in agreement with Townsend et al. [2004].

Table 4.12: The probabilities of absorption to $^1Q_1$ and $^3Q_0$ states and probabilities of intersystem crossing $^3Q_0 \rightarrow ^1 Q_1$ and $^1Q_1 \rightarrow ^3 Q_0$. The values are calculated considering the extreme β-parameters $\beta_{^1Q_1} = -1.0$ and $\beta_{^3Q_0} = +2.0$.

Molecule	CH_3Cl	n-C_3H_7Cl	i-C_3H_7Cl	n-$C_5H_{11}Cl$
$P_{^1A_1 \rightarrow ^1Q_1}$	0.84	0.71	0.62	0.69
$P_{^1A_1 \rightarrow ^3Q_0}$	0.16	0.29	0.38	0.31
$P_{^1Q_1 \rightarrow ^3Q_0}$	0.49	0.58	0.41	0.57
$P_{^3Q_0 \rightarrow ^1Q_1}$	0.68	0.62	0.73	0.62

Conclusion

In presented thesis, we used the VMI experiment to study C–Cl bond photodissociation in chloroalkanes of various chain length and geometry: 1-chloropropane (n-C_3H_7Cl), 2-chloropropane (i-C_3H_7Cl) and 1-chloropentane (n-$C_5H_{11}Cl$), and compared it with the previous investigation of chloromethane (CH_3Cl).

First, the Apparatus for IMaging (where the VMI is implemented) was calibrated using a test system (HBr). Then, the VMI images of Cl and Cl^* photofragments of three higher chloroalkanes were measured, analysed, and compared with the previous analogous measurement of chloromethane. Measured results were also compared with the calculations based on simple classical impulsive models.

Chloroalkanes undergo direct photodissociation and follow two dominant photofragmentation pathways, leading to the ground-state or spin-orbit excited chlorine fragment. After the C–Cl bond is broken, no further fragmentation of the alkyl fragment is possible as it is not energetically accessible. Therefore we assumed a two-body dissociation. The measurements showed that for CH_3Cl less than 10% of the energy available after photodissoiation goes into the internal excitation (vibration and rotation) of the alkyl fragment. In contrast, the internal energy of the alkyl fragment of higher chloroalkanes holds about 40-60% of the available energy. The measured kinetic energies of Cl and Cl^* fragments were close to 0.8 eV for all the chloroalkanes. For higher chloroalkanes, this value is far below the upper limit given by the classical model treating the fragments as hard spheres. CH_3Cl was in good agreement with this model because of the relatively low value of the internal energy of its alkyl fragment. Spectator model approach, assuming quasidiatomic (C–Cl) photodissociation with the rest of the alkyl acting as a (soft) spectator, underestimated the measured kinetic energies of chlorine, but was relatively close to them. In another limit of the spectator model we considered the alkyl being a rigid body. Comparison of these two limits of the spectator classical model with the measured results showed that the photodissociation of higher chloroalkanes probably involves a recoil of a semi-rigid alkyl fragment. Possible partitioning between the rotational and vibrational excitation of the alkyl fragments was briefly discussed, however, such information is not accessible within our measurement setup.

For the analysis of measured anisotropy of Cl and Cl^* fragments we used a simple model proposed by Townsend et al. [2004], however, with corrected β anisotropy parameters. The analysis showed that most of the Cl and Cl^* fragments come from the direct absorption into the singlet state $^1Q_1$. The probability of the direct absorption into the triplet state $^3Q_0$ increases for the higher chloroalkanes, and is especially high for i-C_3H_7Cl (24%). From the analysis, it seems that the position of chlorine group have considerable impact on the probability of direct transition into the triplet state. The calculated intersystem crossing probabilities are 41-58% for singlet-triplet crossing and 80-96% for triplet-singlet crossing, and are the lowest for i-C_3H_7Cl. Measurement and further analysis showed that the change of the chlorine group position has greater effect on the photodissociation dynamics of chloroalkanes than the chain prolongation.

The results of the work were published in a peer-reviewed journal Physical Chemistry Chemical Physics.

Outlook

As has been emphasised many times before, heterogeneous reactions play a crucial role in our atmosphere, and cannot be omitted from the atmospheric models and projections. In this thesis, we have studied and compared the photodissociation dynamics of four selected chloroalkanes of different alkyl chain lengths and chlorine group positions. The next step might be to investigate these chloroalkanes in solvated environment. The theoretical dynamics simulations of Pasalic et al. [2011] showed that the chloromethane is likely to align its methyl group towards the water surface whereas 1-chloropentane prefers different alignment – rather parallel with the alkyl chain pointing slightly to the gas phase. This difference might affect the chemistry of the chloroalkanes of various chain lengths adsorbed on the ice nanoparticles in the atmosphere.

In the CLUster Beam apparatus (CLUB), schematically illustrated in Figure 4.6, it is possible to create water clusters in the molecular beam and pick-up different chloroalkanes in the pick-up chambers. Then, subsequent reactions can be studied by various methods, e.g. VMI or time-of-flight mass spectrometer with reflectron (RTOFMS). Combination of measurements on AIM and CLUB will give us then the complete description of the studied system.

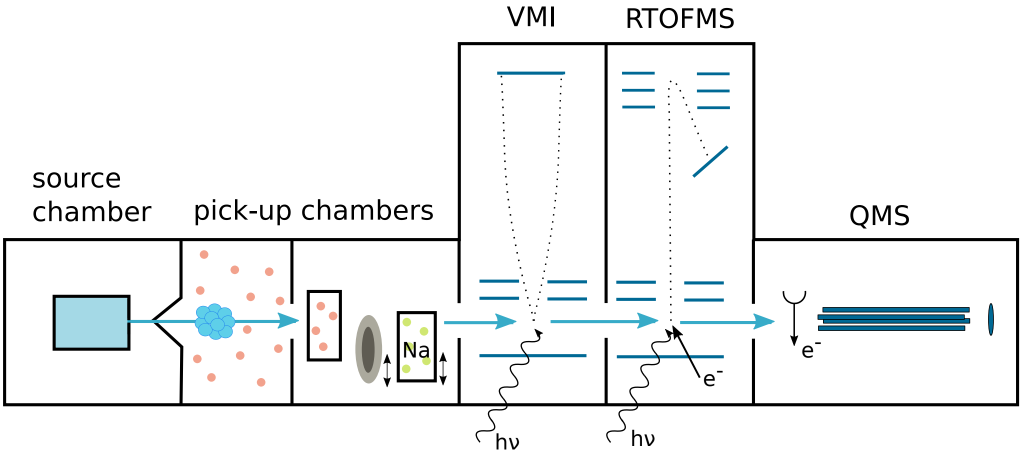

Figure 4.6: CLUB scheme.

Bibliography

S. Arepalli, N. Presser, D. Robie, and R. J. Gordon. Detection of Cl atoms and HCl molecules by resonantly enhanced multiphoton ionization. *Chemial Physics Letters*, 118:88–92, 1985.

E. Bahlmann, F. Keppler, J. Wittmer, M. Greule, H. F. Schöler, R. Seifert, and C. Zetzsch. Evidence for a major missing source in the global chloromethane budget from stable carbon isotopes. *Atmospheric Chemistry and Physics*, 19: 1703–1719, 2019.

S. J. Blanksby and G. B. Ellison. Bond Dissociation Energies of Organic Molecules. *American Chemical Society*, 36(4):255–263, 2003.

C. Bobbert, S. Schütte, C. Steinbach, and U. Buck. Fragmentation and reliable size distributions of large ammonia and water clusters. *The European Physical Journal D*, 19:183–192, 2002.

U. Boesl. Time-of-flight mass spectrometry: Introduction to the basics. *Mass Spectrometry Reviews*, 36(1):86–109, 2016.

R. N. Bracewell. *The Fourier Transform and its Applications.* McGraw-Hill, 2000.

U. Buck and R. Krohne. Cluster size determination from diffractive He atom scattering. *The Journal of Chemical Physics*, 105(13):5408–5415, 1996.

G. E. Busch and K. R. Wilson. Triatomic Photofragment Spectra. I. Energy Partitioning in NO_2 Photodissociation. *The Journal of Chemical Physics*, 56 (7):3626–3638, 1972.

A. W. Castleman. Particle formation: Clusters and nuclei. *Journal of Cluster Science*, 1(1):3–27, 1990.

S. Chakrabarty, J. J. Ferreiro, M. Lippe, and R. Signorell. Toluene Cluster Formation in Laval Expansions: Nucleation and Gowth. *The Journal of Physical Chemistry A*, 121(20):3991–4001, 2017.

D. W. Chandler and P. L. Houston. Two-dimesional imaging of state-selected photodissociation products detected by multiphoton ionization. *The Journal of Chemical Physics*, 87:1445, 1987.

M. E. Corrales, V. Loriot, G. Balerdi, J. González-Vázquez, R. de Nalda, L. Bañares, and A. H. Zewail. Structural dynamics effects on the ultrafast chemical bond cleavage of a photodissociation reaction. *Physical Chemistry Chemical Physics*, 16:8812–8818, 2014.

P. Cristofanelli, J. Arduini, F. Calzolari, U. Giostra, P. Bonasoni, and M. Maione. First Evidences of Methyl Chloride (CH_3Cl) Transport from the Northern Italy Boundary Layer during Summer 2017. *Atmosphere*, 11(3):238–253, 2020.

A. R. Douglass, P. A. Newman, and S. Solomon. The Antarctic ozone hole: An update. *Physics Today*, 67(7):42–48, 2014.

A. T. J. B. Eppink and D. H. Parker. Velocity map imaging of ions and electrons using electrostatic lenses: Application in photoelectron and photofragment ion imaging of molecular oxygen. *Review of Scientific Instruments*, 68:3477, 1997.

D. W. Fahey and M. I. Hegglin. (Coordinating Lead Authors). Twenty Questions and Answers About the Ozone Layer: 2010 Update, Scientific Assessment of Ozone Depletion: 2010. World Meteorological Organization, Geneva, Switzerland, 2011. [Reprinted from Scientific Assessment of Ozone Depletion: 2010, Global Ozone Research and Monitoring Project-Report No. 52, World Meteorological Organization, Geneva, Switzerland, 2011.].

J. Fedor, J. Kočišek, V. Poterya, O. Votava, A. Pysanenko, M. L. Lipciuc, T. N. Kitsopoulos, and M. Fárník. Velocity map imaging of HBr photodissociation in large rare gas clusters. *The Journal of Chemical Physics*, 134:154303, 2011.

J. J. Ferreiro, S. Chakrabarty, B. Schläppi, and R. Signorell. Observation of propane cluster size distributions during nucleation and growth in a Laval expansion. *Journal of Chemical Physics*, 145(21):211907, 2016.

M. Fárník. *Molecular dynamics in free clusters and nanoparticles studied in molecular beams: DSc. thesis in physical chemistry.* ICT Prague Press, Praha, 2011.

M. Fárník. Modern methods in chemical physics II [lecture]. University of Chemistry and Technology, Prague, September 29, 2020.

M. Fárník and J. Lengyel. Mass spectrometry of aerosol particle analogues in molecular beam experiment. *Mass Spectrometry Reviews*, 2017.

M. Fárník, J. Fedor, J. Kočišek, J. Lengyel, E. Pluhařová, V. Poterya, and A. Pysanenko. Pickup and reactions of molecules on clusters relevant for atmospheric and interstellar processes. *Physical Chemistry Chemical Physics*, 23: 3195–3213, 2021.

J. H. Gross. *Mass Spectrometry.* Springer, 2011.

Ø. Hodnebrog, B. Aamaas, J. S. Fuglestvedt, G. Marston, G. Myhre, C. J. Nielsen, and et al. Updated global warming potentials and radiative efficiencies of halocarbons and other weak atmospheric absorbers. *Reviews of Geophysics*, 58:e2019RG000691, 2020.

K. E. Holdy, L. C. Klotz, and K. R. Wilson. Molecular Dynamics of Photodissociation: Quasidiatomic Model for ICN. *The Journal of Chemical Physics*, 52 (9):4588–4599, 1970.

P. L. Houston. Vector correlations in photodissociation dynamics. *The Journal of Physical Chemistry*, 91(21):5388–5397, 1987.

P. Jena and A. W. Castleman. Clusters: A bridge across the disciplines of physics and chemistry. *Proceedings of the National Academy of Sciences*, 103 (28):10560–10569, 2006.

M. Kawasaki, K. Kasatani, H. Sato, H. Shinohara, and N. Nishi. Photodissociation of molecular beams of halogenated hydrocarbons at 193 nm. *Chemical Physics*, 88:135–142, 1984.

F. Keppler, D. B. Harper, R. M. Röckmann, T. Moore, and J. T. G. Hamilton. New insight into the atmospheric chloromethane budget gained using stable carbon isotope ratios. *Atmospheric Chemistry and Physics*, 5:2403–2411, 2005.

C. E. Kolb and D. R. Worsnop. Chemistry and composition of atmospheric aerosol particles. *Annual Review of Physical Chemistry*, 63(1):471–491, 2012.

J. P. Leal, N. Marques, and J. Takats. Bond dissociation enthalpies of U(IV) complexes. An integrated view. *Journal of Organometallic Chemistry*, 632: 209–214, 2001.

S. Li, M. Park, C. O. Jo, and S. Park. Emission estimates of methyl chloride from industrial sourcesin China based on high frequency atmospheric observations. *Journal of Atmospheric Chemistry*, 74(2):227–243, 2017.

J. M. Lobert, W. C. Keene, J. A. Logan, and R. Yevich. Global chlorine emissions from biomass burning: Reactive Chlorine Emissions Inventory. *Journal of Geophysical Research*, 104:8373–8389, 1999.

R. Loudon. *The Quantum Theory of Light*. Oxford University Press, 1983.

M. J. Molina and F. S. Rowland. Stratospheric sink for chlorofluoromethanes: chlorine atom-catalysed destruction of ozone. *Nature*, 249:810–812, 1974.

M. L. Murillo-Sánchez, A. Zanchet, S. M. Poullain, J. González-Vázquez, and L. Bañares. Structural dynamics effects on the electronic predissociation of alkyl iodides. *Scientific reports*, 10(1):1–11, 2020.

NIST, 2021. National Institute of Standards and Technology. https://www.nist.gov/. Accessed June 14, 2021.

Nobel Media AB. The Nobel Prize in Chemistry 1995. `https://www.nobelprize.org/prizes/chemistry/1995/press-release//`. Accessed June 4, 2021.

H. Pasalic, M. Roeselova, and H. Lischka. Methyl and Pentyl Chloride in a Microhydrated Environment and at the Liquid Water-Vapor Interface: A Theoretical Study. *The Journal of Physical Chemistry B*, 115:1807–1816, 2011.

H. Pauly. *Atom, Molecule, and Cluster Beams I: Basic Theory, Production and Detection of Thermal Energy Beams*. Atom, Molecule, and Cluster Beams. Springer, 2000.

T. Peter. Microphysics and heterogeneous chemistry of polar stratospheric clouds. *Annual Review of Physical Chemistry*, 48:785–822, 1997.

PubChem, 2021. National Center for Biotechnology Information. https://pubchem.ncbi.nlm.nih.gov/. Accessed June 14, 2021.

P. M. Regan, S. R. Langford, D. Ascenzi, P. A. Cook, A. J. Orr-Ewing, and M. N. R. Ashfold. Spin–orbit branching in Cl(^{2}P) atoms produced by ultraviolet photodissociation of HCl. *Physical Chemistry Chemical Physics*, 1:3247–3251, 1999.

S. J. Riley and K. R. Wilson. Excited Fragments from Excited Moleules: Energy Partitioning in the Photodissociation of Alkyl Iodides. *Faraday Discussions of the Chemical Society*, 53:132–146, 1972.

R. Schinke. *Photodissociation Dynamics: Spectroscopy and Fragmentation of Small Polyatomic Molecules*. Cambridge Monographs on Atomic, Molecular and Chemical Physics. Cambridge University Press, 1993.

A. E. Siegman. How to (Maybe) Measure Laser Beam Quality. In M. Dowley, editor, *DPSS (Diode Pumped Solid State) Lasers: Applications and Issues*, volume 17, page MQ1. Optical Society of America, 1998.

H. Slaper, G. J. M. Velders, J. S. Daniel, F. R. de Gruijl, and J. C. van der Leun. Estimates of ozone depletion and skin cancer incidence to examine the Vienna Convention achievements. *Nature*, 384:256–258, 1996.

A. G. Smolin, O. S. Vasyutinskii, G. G. Balint-Kurti, and A. Brown. Photodissociation of HBr. 1. Electronic Structure, Photodissociation Dynamics, and Vector Correlation Coefficients. *The Journal of Physical Chemistry A*, 110 (16):5371–5378, 2006.

S. Solomon. Stratospheric ozone depletion: A review of concepts and history. *Reviews of Geophysics*, 37(3):275–316, 1999.

W. R. Stevens, A. Bodi, and T. Baer. Dissociation Dynamics of Energy Selected, Propane, and i-$C_3H_7X^+$ Ions by iPEPICO: Accurate Heats of Formation of i-$C_3H_7^+$, i-C_3H_7Cl, i-C_3H_7Br, and i-C_3H_7I. *The Journal of Physical Chemistry A*, 114(42):11285–11291, 2010.

J. P. Toennies and A. F. Vilesov. Superfluid Helium Droplets: A Uniquely Cold Nanomatrix for Molecules and Molecular Complexes. *Angewandte Chemie International Edition*, 43(20):2622–2648, 2004.

D. Townsend, S. K. Lee, and A. G. Suits. DC Slice Imaging of CH_3Cl Photolysis at 193.3 nm. *The Journal of Physical Chemistry A*, 108(39):8106–8114, 2004.

C. Vallance. *Astrochemistry: From The Big Bang To The Present Day*. World Scientific Publishing Europe Ltd., 2017.

I. S. Vinklárek, J. Rakovský, V. Poterya, and M. Fárník. Different Dynamics of CH_3 and Cl Fragments from Photodissociation of CH_3Cl in Clusters. *The Journal of Physical Chemistry A*, 124:7633–7643, 2020a.

I. S. Vinklárek, J. Rakovský, V. Poterya, and M. Fárník. Clustering and multiphoton effects in velocity map imaging of methyl chloride. *Molecular Physics*, 119:e1823507, 2020b.

I. S. Vinklárek, J. Suchan, J. Rakovský, K. Moriová, V. Poterya, P. Slavíček, and M. Fárník. Energy partitioning and spin–orbit effects in the photodissociation of higher chloroalkanes. *Physical Chemistry Chemical Physics*, 23:14340–14351, 2021.

B. J. Whitaker, editor. *Imaging in molecular dynamics: technology and applications (a user's guide).* Cambridge University Press, 2003.

W. C. Wiley and I. H. McLaren. Time-of-Flight Mass Spectrometer with Improved Resolution. *Review of Scientific Instruments*, 26(12):1150–1157, 1955.

R. Zare and D. R. Herschbach. Doppler Line Shape of Atomic Fluorescence Excited by Molecular Photodissociation. *Proceedings of the IEEE*, 51(1):173–182, 1963.

R. Zimmermann and L. Hanley, editors. *Photoionization and Photo-Induced Process in Mass Spectrometry.* Wiley-VCH, 2021.

List of Abbreviations

AIM	Apparatus for IMaging
CCD	charge-coupled device
CFC	chlorofluorocarbon
CLUB	CLUster Beam apparatus
EI	electron ionization
FWHM	full width at half maximum
IR	infrared
KED	kinetic energy distribution
MCP	micro-channel plate
NIST	National Institute of Standards and Technology
ODS	ozone-depleting substance
OPO	optical parametric oscillator
PES	potential energy surface
PSC	polar stratospheric cloud
QMS	quadrupole mass spectrometer
REMPI	resonance-enhanced multiphoton ionization
RTOFMS	time-of-flight mass spectrometer with reflectron
TOF	time-of-flight
UV	ultraviolet
VMI	velocity map imaging

A. Attachments

A.1 Cartesian coordinates of chloroalkanes

Cartesian coordinates of measured chloroalkanes in units of ångström. Calculation provided by Petr Slavíček and Jiří Suchan (University of Chemistry and Technology, Prague).

CH_3Cl

C	0.000000	0.000000	0.000000
Cl	0.000000	0.000000	1.859263
H	1.026662	0.000000	-0.326801
H	-0.513334	-0.889113	-0.326804
H	-0.513332	0.889119	-0.326789

n-C_3H_7C

C	0.000000	0.000000	0.000000
Cl	0.000000	0.000000	1.856991
C	1.410968	0.000000	-0.562605
C	1.386548	-0.009959	-2.092373
H	2.394504	-0.006780	-2.492718
H	0.882677	-0.893605	-2.474499
H	0.872563	0.862708	-2.486110
H	1.941424	0.875677	-0.203792
H	1.945977	-0.868267	-0.192859
H	-0.552531	-0.880640	-0.291790
H	-0.552414	0.880722	-0.291777

i-C_3H_7Cl

C	0.000000	0.000000	0.000000
Cl	0.000000	0.000000	1.866759
C	1.435448	0.000000	-0.499286
C	-0.817096	-1.180249	-0.499456
H	-0.366915	-2.120154	-0.200226
H	-1.829590	-1.148889	-0.116583
H	-0.861105	-1.152305	-1.585163
H	-0.487141	0.929367	-0.256816
H	1.437489	0.045649	-1.585237
H	1.984219	0.853730	-0.121189
H	1.953484	-0.902487	-0.194939

n-$C_5H_{11}Cl$

C	0.000000	0.000000	0.000000
Cl	0.000000	0.000000	1.856750
C	1.410892	0.000000	-0.562061
C	1.394827	-0.013612	-2.093191
C	2.796902	0.001758	-2.703962
C	2.780040	-0.022992	-4.231733
H	3.788013	-0.008896	-4.635139
H	2.287222	-0.916738	-4.604841
H	2.251387	0.837469	-4.633010
H	3.359387	-0.853200	-2.334832
H	3.327729	0.887889	-2.362555
H	0.861637	-0.896663	-2.442758
H	0.836017	0.846772	-2.459066
H	1.946527	-0.867286	-0.188588
H	1.940379	0.877266	-0.203212
H	-0.553312	-0.880465	-0.290403
H	-0.552846	0.880762	-0.290334

A.2 Published article

Title: Energy partitioning and spin-orbit effects in the photodissociation of higher chloroalkanes
Authors: Ivo S. Vinklárek, Jiří Suchan, Jozef Rakovský, Kamila Moriová, Viktoriya Poterya, Petr Slavíček and Michal Fárník
Journal: *Physical Chemistry Chemical Physics*
First published: June 7, 2021
DOI: 10.1039/D1CP01371H

This attachment was removed from the version stored in public digital repository due to copyright conditions. The full version of the published article can be found here: https://doi.org/10.1039/D1CP01371H.